2-21-2006

Synthesis of low k1 projection lithography utilizing interferometry

Frank Cropanese

Synthesis of low k1 projection lithography utilizing interferometry

by

Frank C. Cropanese, Jr.
B.S. Microelectronics Engineering
Rochester Institute of Technology
(2002)

A thesis submitted in partial fulfillment of the
requirements for the degree of Master of Science
in the Chester F. Carlson Center for Imaging Science
of the College of Science
Rochester Institute of Technology

November 2005

Signature of the Author _____
Date

Accepted by _____
Coordinator, M.S. Degree Program Date

CHESTER F. CARLSON
CENTER FOR IMAGING SCIENCE
COLLEGE OF SCIENCE
ROCHESTER INSTITUTE OF TECHNOLOGY
ROCHESTER, NEW YORK

CERTIFICATE OF APPROVAL

M.S. DEGREE THESIS

The M.S. Degree Thesis of
Frank C. Cropanese, Jr.
has been examined and approved by the
thesis committee as satisfactory for the
thesis requirement for the
Master of Science degree

Dr. Bruce W. Smith, Thesis Advisor Date

Dr. Roger Easton, Committee Member Date

Prof. Dale Ewbank, Committee Member Date

THESIS RELEASE PERMISSION
ROCHESTER INSTITUTE OF TECHNOLOGY
CHESTER F. CARLSON
CENTER FOR IMAGING SCIENCE

Title of Thesis: Synthesis of low k1 projection lithography utilizing interferometry

I, Frank C. Cropanese, Jr., hereby grant permission to the Wallace Memorial Library of R.I.T. to reproduce my thesis in whole or part. Any reproduction will not be for commercial use or profit.

Signature: _____

Date: _____

Synthesis of low k1 projection lithography utilizing interferometry

by

Frank C. Cropanese, Jr.
Submitted to the Chester F. Carlson
Center for Imaging Science
College of Science
in partial fulfillment of the requirements
for the degree of Master of Science
at the Rochester Institute of Technology

Abstract

Interference lithography has been widely utilized as a tool for the evaluation of photoresist materials, as well as emerging resolution enhancement techniques. The interferometric approach is both simple and inexpensive to implement, however it is limited in its ability to examine the impact of defocus due to the inherently large DOF (Depth-of-Focus) in two-beam interference. Alternatively, the demodulation of the aerial image that occurs as a result of defocus in a projection system may be synthesized using a two pass exposure with the interferometric method. The simulated aerial image modulation for defocused projection systems has been used to calculate the single beam exposure required to reproduce the same level of modulation in an interferometric system and a graphical representation termed “Modulation Transfer Curve” (MTC) was subsequently developed. An interferometric exposure system was used to experimentally synthesize defocus for modulations of 0.3, 0.5, 0.7 and 1.0. Feature sizes of 90nm were evaluated across dose and synthetic focus.

Acknowledgements

I would like to extend my eternal gratitude to my thesis advisor, Dr. Bruce W. Smith, who first introduced me to optical lithography many years ago and has given me the opportunity to work on some of the most exciting projects in the field. This thesis is the culmination of a number of discussions I have had with Dr. Smith since joining his research group. His advice and guidance has given me a unique perspective of lithography, which has allowed me countless opportunities to expand my knowledge of the subject.

I also want to thank Dr. Roger Easton and Professor Dale Ewbank for the knowledge and expertise they have shared with me over the past few years. Much of what they have been able to teach me was accomplished through many noteworthy discussions on optics and imaging. I greatly appreciate all the time they have spent with me working on some of the finer details of this work.

My special thanks to the people that made this journey more than just an academic exercise: Anatoly Bourov, Yongfa Fan, Lena Zavyalova, Neal Lafferty, Jianming Zhou and Andrew Estroff. They made the hours of research fly by with frequent trips for coffee and outlandish conversations when the days were moving slow.

And finally, my close friends and family who have supported me from the beginning and continue to encourage any ridiculous ideas or absurd inklings that I may spawn.

Dedication

I am dedicating this thesis to the loving memory of the two most influential people to have been a part of my life, my grandmother Isabella Cropanese and my grandfather Thomas Duffy. They gave me the strength and resolve to face each day with optimism and patience. They showed me how my words and actions could shape those around me for better or worse, and how the right combination could bring a smile. They taught me what it truly took to be a good human being in a world that doesn't always make it easy. Though they never passed on any of these things directly, the examples they set will guide me the rest of my life.

Table of Contents

List of Figures

List of Tables

List of Acronyms

CD	Critical Dimension
NA	Numerical Aperture
DOF	Depth of Focus
RET	Resolution Enhancement Technology
IL	Interferometric Lithography
LIL	Liquid Immersion Lithography
FT	Fourier Transform
PSF	Point Spread Function
OTF	Optical Transfer Function
OPD	Optical Path Difference
TCC	Transmission Cross Coefficient
AR	Anti-Reflective
TMAH	TetraMethyl Ammonium Hydroxide
SEM	Scanning Electron Microscope
AI	Aerial Image
EL	Exposure Latitude

1 Introduction to optical lithography

The fabrication capabilities of the semiconductor industry are continually progressing toward smaller feature sizes, also known as critical dimensions (*CD*'s). The effort is driven by the demand for faster microprocessors. The burden of delivering smaller critical dimensions has been placed on lithographers, who in turn have produced a number of novel techniques to extend optical lithography as the principal means of imaging. The smallest *CD* that can be resolved is determined by optical diffraction and is mathematically represented in the Rayleigh criterion, which is expressed as a function of the exposing wavelength λ and the numerical aperture $(NA = n\sin\theta)$, where n is the refractive index of the imaging medium and θ is the maximum acceptance angle. The resulting expression for the critical dimension is:

$$CD = k_1 \frac{\lambda}{NA} \tag{1.1}$$

where k_1 is a scaling factor that accounts for variations in the lithography process. Such variations are present due to photoresist processing, coherence of the illumination and wavefront manipulation. Physical limitations constrain k_1 to be greater than 0.5 and 0.25 for coherent and incoherent illumination, respectively [1].

Examination of equation (1.1) leads to the conclusion that the critical dimension can be reduced by altering any of the three parameters k_1, λ, and/or *NA*. Decreasing the process dependent factor k_1 is the most cost-effective method of resolution enhancement.

A significant development effort would be required to shorten λ, and an increase *NA* would necessitate fabrication of projection lenses with minimal aberrations. The k_1 factor may be reduced by engineering the wavefront to improve the spatial frequency information of the object being imaged. This may be performed either in the spatial domain (at the mask plane), or in the frequency domain (via pupil filtering). There are relative advantages and disadvantages to both methods, but the resulting enhancement of the aerial image may be comparable in either case. Some typical methods for k_1 optimization include illumination coherence and phase shift masking. Frequency analysis is of considerable concern when implementing some of the Resolution Enhancement Technologies (RET) that have been developed over recent years to address the need for k_1 optimization [1].

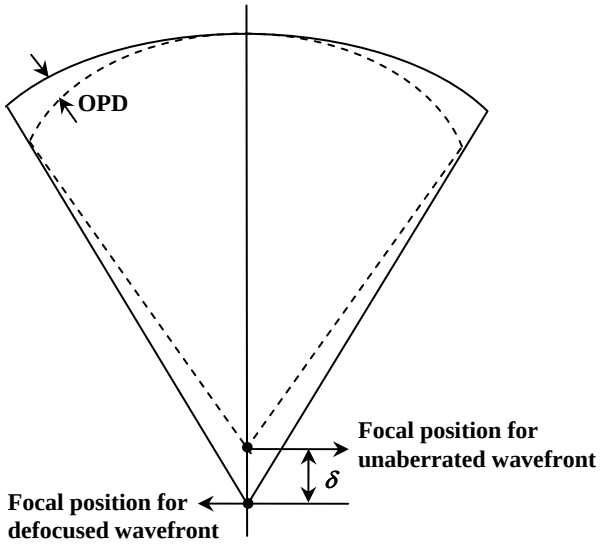

Figure 1. Focal positions of unaberrated (dashed) and defocused (solid) wavefront. The optical path difference (OPD) introduces a delta in the focal positions of δ.

The depth of focus *(DOF)* is one figure of merit that must be considered when attempting to optimize the resolution of an imaging system. The *DOF* is characterized as the usable range of field positions along the optical axis that result in minimal image degradation. The functional form of the *DOF* is:

$$DOF = \pm k_2 \frac{\lambda}{NA^2} \tag{1.2}$$

It is readily evident from equation (1.2) that an undesirable reduction in the *DOF* will occur when optimizing resolution through the use of short wavelengths or high *NA*. The functional form of the *DOF* also includes a process dependent factor analogous to the factor incorporated into the Rayleigh criterion for resolution. The term k_2 is introduced to account for all process variables not related to wavelength or numerical aperture, and is typically $k_2 \approx 0.5$. A large DOF is desired in order to minimize the impact of defocus aberration on an imaging system [1].

Imaging through the use of optical pattern transfer techniques relies on the magnitude and phase information that are generated by passing illumination with spectral bandwidth ($\Delta\lambda$) centered about λ in the UV, through an object (or reticle) at the mask plane. The magnitude and phase beyond the mask plane are characterized by the spatial distribution of the resultant electromagnetic field that is created upon diffraction at the reticle. Only a portion of the frequency information associated with the electromagnetic field is captured since the projection lens acts as a low-pass filter by limiting the frequency content of the recorded image.

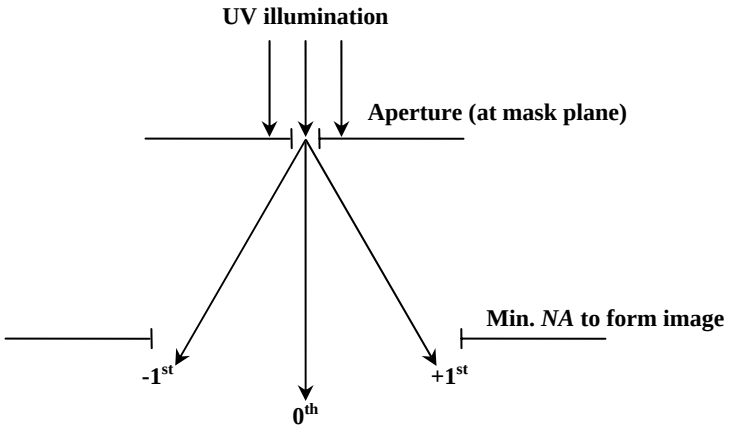

Figure 2. Diagram of UV illumination diffraction upon encountering an aperture. At least the $\pm 1^{st}$ diffraction orders must be captured by the projection lens *NA* to form an image.

Typically, a minimum of the 1^{st}-order frequencies (first diffraction orders) must be collected to adequately reproduce the object at the image plane. The 0^{th} diffraction order is a zero frequency term that is generally incorporated to apply a DC bias to the image intensity distribution created by higher frequencies. The variety of mask configurations, illumination conditions and aberrations that are used with projection imaging systems generate unique 0^{th} and 1^{st} diffraction orders that can have a significant impact on lithographic performance. The evaluation of different system configurations can be a cumbersome and costly task; however, it is possible to synthesize the resulting behavior by utilizing a simple interferometric lithography system.

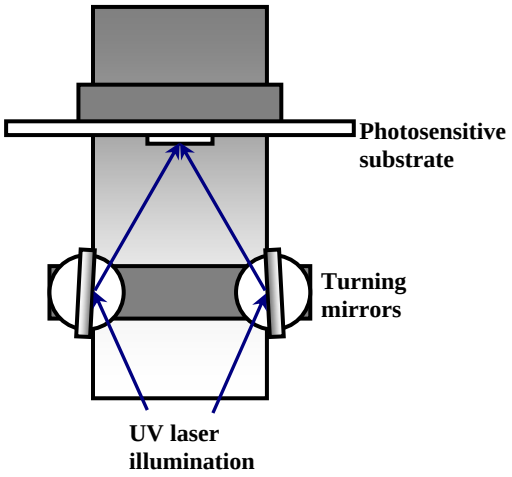

Figure 3. Generic diagram of an interferometric lithography (IL) exposure system.

Interferometric lithography (IL) is accomplished by interfering two mutually coherent light beams at the surface of a photosensitive substrate to produce a sinusoidal intensity distribution. Attenuation of one of these beams will re-create some of the conditions that exist in a typical lithography system, such as phase shift masking and illumination coherency [12]. The same procedure can be extended to synthesize deviations from ideal image formation (such as defocus) by appropriately adjusting the relative intensity of the two interfering beams. Interferometric lithography systems are currently capable of reproducing only simple periodic structures and will synthesize projection lithography with a limited degree of tolerable error. The synthesis of typical deviations from ideal behavior in projection lithography, such as defocus, enables interferometric lithography to be a valuable research tool.

2 Wave theory and projection optics

An understanding of the fundamentals of light propagation and diffraction is of considerable value when examining the properties of optical lithography image formation. The following discussion, derived from treatments by Smith [1], Goodman [2] and Gaskill [3], will cover the basic scalar diffraction theory of wave propagation, Fraunhofer diffraction and propagation through a typical optical system for projection lithography. Subtle approximations can be made at key steps in the analysis that will allow substantial simplification, which are discussed in this chapter. Further consideration will be paid to the ability to synthesize the function of projection systems utilizing single beam attenuation in two-beam interferometric lithography.

2.1 Scalar diffraction theory

Diffraction is the direct result of the wave nature of light and can be explained by the principle of wave propagation that was postulated by Huygens in 1678. Diffraction occurs whenever the lateral extent of a light wave is restricted by an obstruction (an aperture) provided that the size of the opening is of the order of the illumination wavelength. Huygens' Principle states that a wavefront may be modeled as an infinite number of secondary point disturbances that produce spherical "wavelets" and that the properties of the original wavefront at any point in space and time can be derived from the mutual interference of the secondary wavelets. This model explained, in part, the

existence of light and dark fringes within the geometric shadow of an illuminated aperture. It also set the stage for later discoveries involving interference and diffraction.

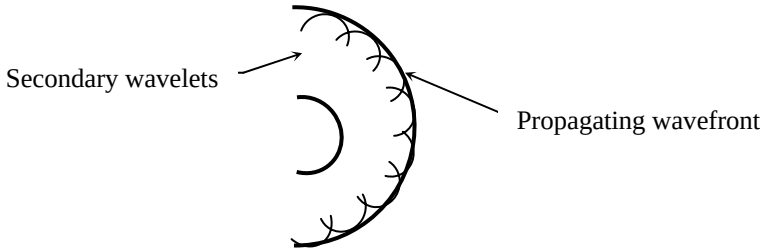

Figure 4. Huygens' Principle - The superposition of secondary wavelets to construct a propagating wavefront.

The development of a cohesive theory of diffraction requires a number of major simplifications and approximations. The most significant assumption is that light can be treated as a purely scalar phenomenon and therefore the vector properties of electromagnetic fields, such as polarization, can be neglected. The two primary requirements when utilizing a scalar approach to diffraction are (a) the aperture must be relatively large when compared with the exposing wavelength and (b) the diffracted illumination must not be examined in close proximity to the aperture, rather observation should occur in the "Fraunhofer diffraction region". This ensures that the coupling effects of the boundary conditions on the electric and magnetic field vectors are minimized and allows the components of the analyisis to be treated as lumped elements with simple properties. [2]

The electric and magnetic field vectors of a propagating wave are represented by $\vec{E}$ and $\vec{B}$, respectively, which are both functions of three spatial coordinates and time.

A light wave propagating through a medium that is linear, isotropic, homogenous and nondispersive must satisfy the wave equation for both the electric and magnetic fields:

$$\text{(a)}\ \ \nabla^2\vec{E} = \mu_o\varepsilon_o\frac{\partial^2\vec{E}}{\partial t^2} \qquad \text{(b)}\ \ \nabla^2\vec{B} = \mu_o\varepsilon_o\frac{\partial^2\vec{B}}{\partial t^2} \tag{2.1}$$

where the constants μ and ε are correspondingly the permeability and permittivity of the propagating medium. The spatial variation of the wave is the primary concern, therefore the scalar approximation to the wave equations may be used and any temporal dependence may be dropped. The approximation takes the form of the Helmholtz equation:

$$\text{(a)}\ \ \left(\nabla^2 + k\right)E = 0 \qquad \text{(b)}\ \ \left(\nabla^2 + k\right)B = 0 \tag{2.2}$$

where *k* is the wave number given by $k = 2\pi/\lambda$ and λ is the wavelength of illumination. *E* and *B* are the scalar electric and magnetic fields, respectively.

An additional mathematical relation known as Green's theorem is required to determine the amplitude of a propagating wavefront at any point in space. Green's theorem relates the Laplacian, or gradient of two scalar fields:

$$\iiint_V \left(\psi\,\nabla^2\varphi - \varphi\,\nabla^2\psi\right)dV = \iint_S \left(\psi\,\vec{\nabla}\varphi - \varphi\,\vec{\nabla}\psi\right)d\vec{a} \tag{2.3}$$

where $\psi = \vec{E}(\vec{r})$ is a wave propagating in space, $\varphi = e^{-ikr}/r$ is an expanding spherical wave, and *r* is the magnitude of a vector pointing from the optical disturbance to the observation point. The waves ψ and φ are solutions to the scalar Helmholtz equation.

The solution to the surface integration is known as the Helmholtz-Kirchoff integral theorem:

$$\psi = \frac{1}{4\pi}\iint_S \left(\varphi \frac{\partial \psi}{\partial n} - \psi \frac{\partial \varphi}{dn} \right) ds \tag{2.4}$$

This equation allows for the determination of the field of a propagating wave given boundary conditions for a surface surrounding the observation point. The directional derivative $\partial/\partial n$ is directed along the outward normal to the bounding surfaces. If the scalar assumption is applicable, the terms φ and ψ are solutions to the scalar Helmholtz equation and the Sommerfeld radiation condition is satisfied then equation (2.4) is valid. The Sommerfeld radiation condition requires that the optical disturbance ψ vanish as fast as the amplitude and phase of a diverging spherical wave, thus guaranteeing that only outgoing waves encounter the bounding surface. The Rayleigh-Sommerfeld solution to the Helmholtz-Kirchoff integral theorem is the summation of all wavelets of a propagating wavefront evaluated at any point in space:

$$\psi\left(\vec{r}_1\right) = \frac{1}{i\lambda}\iint_S \frac{\psi\left(\vec{r}_0\right)\exp\left(ikr_{10}\right)}{r_{10}}\, ds \tag{2.5}$$

This expression will be used to derive a functional form for the Fraunhofer diffraction of a propagating light wave.

2.2 Fresnel and Fraunhofer diffraction

The Rayleigh-Sommerfeld solution can be represented in rectangular coordinates for the explicit situation of the diffracting aperture in the x-y plane and illuminated by light propagating in the positive z-direction, as shown in Figure 5. The propagation of light from the diffracting aperture over a distance z_1 is:

$$\psi(x,y) = \frac{1}{i\lambda}\int_{-\infty}^{\infty}\int \psi(x_o, y_o; z=0)\frac{\exp\left(ik\left|R_1 - R_o\right| - \omega t\right)}{\left|R_1 - R_o\right|}dx_o dy_o \tag{2.6}$$

where $k = 2\pi/\lambda$, ω is the temporal frequency, and t is the time of propagation.

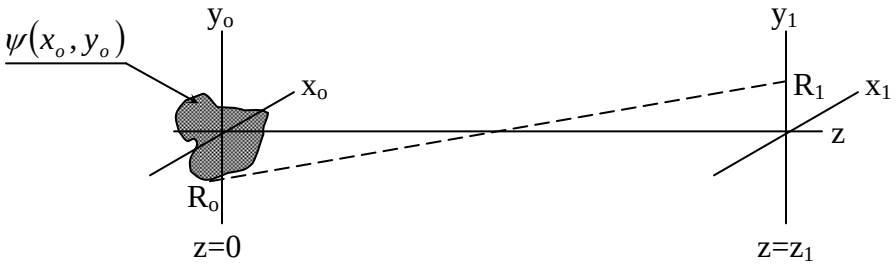

Figure 5. Geometry of a diffracted wavefront traveling in the +z-direction.

$$\left|R_1 - R_0\right| = \sqrt{z_1^2 + (x_o - x_1)^2 + (y_o - y_1)^2} = z_1\left[1 + \frac{(x_o - x_1)^2 + (y_o - y_1)^2}{z_1^2}\right]^{1/2} \tag{2.7}$$

If x_o, x_1, y_o and y_1 are restricted to sufficiently small values to ensure that the quadratic term in equation (2.7) is much smaller than one, then the denominator may be expanded using a Binomial series approximation:

$$(1+x)^n = 1 + nx + \frac{n(n-1)x^2}{2} + \cdots \tag{2.8}$$

where $n = \frac{1}{2}$. Equation (2.6) then becomes the Fresnel approximation to diffraction, given in equation (2.9) where an additional term is added in the exponential factor in the Binomial series, while the approximation in the denominator retains fewer components because the exponential term is more significant:

$$\psi(x,y) = \frac{\exp(i\omega t)}{i\lambda}\int\int_{-\infty}^{\infty}\psi(x_o,y_o)\frac{\exp\left(ik\left[z_1 + \frac{(x_o - x_1)^2 + (y_o - y_1)^2}{2z_1}\right]\right)}{z_1}dx_o dy_o \qquad (2.9)$$

$$= \frac{\exp(i(kz_1 - \omega t))}{i\lambda z_1}\int\int_{-\infty}^{\infty}\psi(x_o,y_o)\exp\left(i\pi\left[\frac{(x_o - x_1)^2 + (y_o - y_1)^2}{\lambda z_1}\right]\right)dx_o dy_o$$

The Fresnel approximation takes the form of a convolution of the input amplitude $\psi(x_o, y_o)$ with the impulse response, given by $h(x_o, y_o)$.

$$h(x_o,y_o) = \frac{\exp(i(kz_1 - \omega t))}{i\lambda z_1}\exp\left(i\pi\left[\frac{x_o^2 + y_o^2}{\lambda z_1}\right]\right) \qquad (2.10)$$

The convolution in equation (2.9) suggests that Fresnel diffraction is a result of the Fourier Transform of the product of the complex field distribution, just beyond the aperture, and a quadratic phase factor. Fresnel diffraction is applicable when observation is occurring in the near field of the aperture. A critical factor when considering the accuracy of the Fresnel approximation is the substitution of spherical wavelets with parabolic wavefronts. The accuracy of this substitution is ultimately determined by the number of terms retained in the binomial expansion.

The Fraunhofer approximation to diffraction can be derived after expanding the exponential in equation (2.9) under the condition that the distance propagated z_1 is larger yet:

$$z_1 >> \frac{x_o^2 + y_o^2}{2z_1} \tag{2.11}$$

The approximate field can then be expressed as:

$$\psi(x,y) = C \cdot \int_{-\infty}^{\infty}\int \psi(x_o, y_o) \exp\left(-i\frac{2\pi}{\lambda z_1}(x_o x_1 + y_o y_1)\right) dx_o dy_o = C \cdot \Psi\left(\frac{x_1}{\lambda z_1}, \frac{y_1}{\lambda z_1}\right) \tag{2.12}$$

$$C = \frac{1}{i\lambda z_1} \exp\left(i\frac{2\pi z_1}{\lambda}\right) \exp\left(i\frac{\pi}{\lambda z_1}\left(x_1^2 + y_1^2\right)\right)$$

where Ψ is the 2-D Fourier transform of ψ. The Fourier transform of an arbitrary function in rectangular coordinates takes the form:

$$F(\xi,\eta) = \int_{-\infty}^{\infty}\int f(x,y) \exp\left(-i\,2\pi(\xi x + \eta y)\right) dx\,dy \tag{2.13}$$

where ξ and η are spatial frequencies and *x* and *y* are rectangular space coordinates. The integrand in equation (2.12) allows the distribution of light in the Fraunhofer diffraction region to be approximated as the product of the Fourier transform of the diffracting aperture and a constant phase factor *C*, where the Fourier transform of $\psi(x_o, y_o)$ is defined as $\Psi\left(\frac{x_1}{\lambda z_1}, \frac{y_1}{\lambda z_1}\right)$. The terms $\frac{x_1}{\lambda z_1}$ and $\frac{y_1}{\lambda z_1}$ have dimensions of spatial frequency, identical to the ξ and η terms found in the Fourier transform integral.

2.3 Propagation in projection optics

A propagating wave that passes through a lens element can be mathematically expressed as the product of the wave amplitude and the complex pupil function of the lens. This function includes the aperture size and change in phase due to the focusing action of the lens. The focusing power of an aberration-free positive lens is due to a negative quadratic phase factor added to the incident wavefront. The reshaping of the propagating wavefront may be utilized to perform a Fourier transform of the incident intensity distribution. This transformation serves as a valuable tool for optical system engineers. It can be shown that the two-dimensional Fourier transform is produced at the back focal plane of the lens due to an input placed in front of the lens. This action is comparable to wave propagation in the Fraunhofer diffraction region except that it contains some additional constant phase terms. The transformation of the wavefront can be mathematically approximated by:

$$t(x,y) = \exp\left(i\frac{2\pi}{\lambda} n t_{\max} \right) \exp\left[-\frac{i\pi}{\lambda}(n-1)\left(\frac{1}{R_1} - \frac{1}{R_2} \right)\left(x^2 + y^2 \right) \right] \qquad (2.14)$$

where the lens properties are denoted by the refractive index n, the maximum thickness t_{max} and the front and rear radii of curvature, R_1 and R_2 respectively. Equation (2.14) is a valid approximation provided that the region of interest on the wavefront, propagating left to right, is restricted to the paraxial region (a sufficiently small area surrounding the optical axis). The sign convention for the radii R_1 and R_2 in equation (2.14) is shown in Figure 6 such that convex surfaces (center of curvature to the right of surface) have a

positive radius of curvature and concave surfaces (center of curvature to the left of the surface) have a negative radius of curvature.

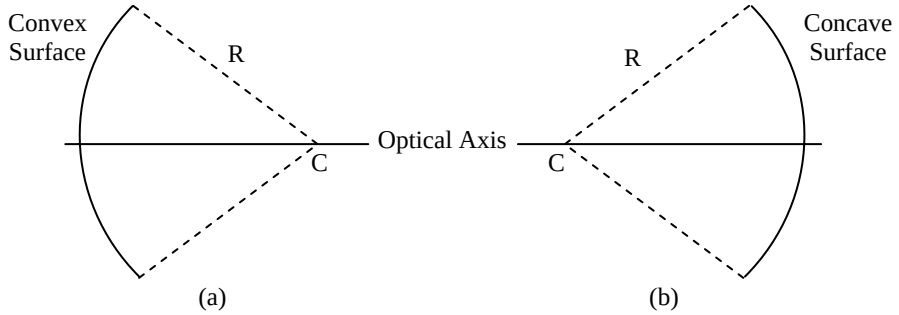

Figure 6. Sign convention for (a) convex (center of curvature C to the left) and (b) concave surfaces (center of curvature C to the right).

All of the lens properties in equation (2.14) can be combined to form the lensmaker's equation:

$$\frac{1}{f} = (n-1)\left(\frac{1}{R_1} - \frac{1}{R_2}\right) \tag{2.15}$$

This conveniently allows the equation to be simplified through the substitution of the focal length *f* of the lens.

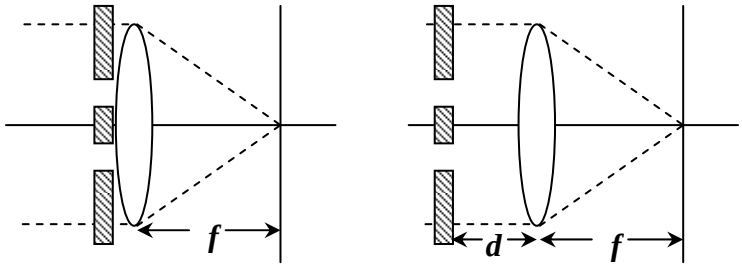

Figure 7. Input distribution impinging on a positive lens element with the input (a) against the front of the lens and (b) at a distance *d* in front of the lens. The focal length of the lens is denoted by *f*.

Consider the two optical configurations in Figure 7. These will be examined to derive the Fourier transforming properties of a lens. In Figure 7(a), monochromatic spatially coherent light is passed through an object placed in contact with the front surface of the lens element. The field distribution immediately in front of the lens is given by $\psi_{lens}(x_o, y_o)$ and the distribution immediately after the lens $\psi_{lens}(x_o, y_o)$ is found by multiplying the phase applied by the lens giving:

$$\psi'_{lens}(x_o, y_o) = \psi_{lens}(x_o, y_o) \cdot P(x_o, y_o) \cdot \exp\left[-\frac{\pi}{\lambda f}\left(x_o^2 + y_o^2\right)\right] \tag{2.16}$$

where $P(x_o, y_o)$ is the lens pupil function that restricts the lateral extent of the field distribution. If the field distribution in equation (2.16) is propagated a distance equivalent to the focal length of the lens, the field at that plane may be calculated by applying the Fresnel diffraction approximation in equation (2.9) with $z_1 = f$:

$$\begin{aligned}\psi_f(x_1, y_1) = \frac{1}{i\lambda f}\exp\left[\frac{i\pi}{\lambda f}\left(x_1^2 + y_1^2\right)\right] \\ \cdot \int_{-\infty}^{\infty}\int \psi'_{lens}(x_o, y_o)\exp\left[\frac{i\pi}{\lambda f}\left(x_o^2 + y_o^2\right)\right]\exp\left[-\frac{i\pi}{\lambda f}\left(x_o x_1 + y_o y_1\right)\right]dx_o dy_o\end{aligned} \tag{2.17}$$

Upon substitution of equation (2.16) into equation (2.17), the quadratic phase terms cancel and the distribution at the back focal plane becomes the Fourier transform of the input:

$$\psi_f(x_1, y_1) = \frac{1}{i\lambda f}\exp\left[\frac{i\pi}{\lambda f}\left(x_1^2 + y_1^2\right)\right] \cdot \int_{-\infty}^{\infty}\int \psi_{lens}(x_o, y_o)\exp\left[-\frac{i\pi}{\lambda f}\left(x_o x_1 + y_o y_1\right)\right] dx_o dy_o \tag{2.18}$$

plus an additional constant quadratic phase factor that will be neglected assuming the lens pupil $P(x_o, y_o)$ is much larger than the impinging area of the input. The complex field distribution after passing through a lens and propagating the distance *f* equal to the focal length of that lens is equivalent to propagation in the Fraunhofer diffraction region. Therefore, the distribution seen at the back focal plane is approximately the Fraunhofer diffraction pattern.

The second configuration, Figure 7(b), assumes that the input object is placed a distance *d* in front of the lens. In this situation, the field distribution must propagate the distance *d* to the lens, interact with the lens and then propagate to the back focal plane. From equation (2.10), it is shown that the action of propagation in the Fresnel diffraction region is mathematically represented by a convolution of the field distribution with the impulse response $h(x_o, y_o)$. The result of this convolution will be the field distribution immediately in front of the lens. The Fourier transform of this convolution approximates the field distribution at the back focal plane, since it was learned from the first configuration that an object placed in contact with the front of a positive lens will have its Fourier transform projected to the back focal plane of that lens. The Fourier transform of this convolution is:

$$\psi(x_o, y_o) * h(x_o, y_o) \xrightarrow[\substack{x_o \to x_1 \\ y_o \to y_1}]{F.T.} \Psi\left(\frac{x_1}{\lambda d}, \frac{y_1}{\lambda d}\right) \cdot \exp\left[-\frac{i\pi}{\lambda d}\left(x_1^2 + y_1^2\right)\right] \tag{2.19}$$

where the Fourier transform operation is denoted by "*FT*". This result is then multiplied by the quadratic phase factor similar to that in equation (2.18).

$$\psi_f(x_1, y_1) = \Psi\left(\frac{x_1}{\lambda d}, \frac{y_1}{\lambda d}\right) \cdot \exp\left[-\frac{i\pi}{\lambda d}\left(x_1^2 + y_1^2\right)\right] \cdot \frac{1}{i\lambda f} \exp\left[\frac{i\pi}{\lambda f}\left(x_1^2 + y_1^2\right)\right] \tag{2.20}$$

After consolidation of the quadratic phase factors and recasting of the term $\Psi\left(\frac{x_1}{\lambda d}, \frac{y_1}{\lambda d}\right)$ into integral form, the distribution at the back focal plane is:

$$\begin{aligned} \psi_f(x_1, y_1) = \frac{1}{i\lambda f} \exp\left[\frac{i\pi}{\lambda f}\left(1 - \frac{d}{f}\right)\left(x_1^2 + y_1^2\right)\right] \\ \cdot \int_{-\infty}^{\infty}\int \psi(x_o, y_o) \exp\left[-\frac{i\pi}{\lambda f}\left(x_o x_1 + y_o y_1\right)\right] dx_o dy_o \end{aligned} \tag{2.21}$$

The output distribution is again related to the frequency spectrum of the input, as seen in the first configuration of Figure 7(a). However, the result here has a more complicated quadratic phase term preceding the integral. This phase term is eliminated by placing the input at the front focal plane of the lens, so that *d=f*.

Köhler illumination is the typical optical configuration utilized in optical systems for microlithography. The images of two objects, the reticle and source, are simultaneously transmitted [1]. The Köhler system can be modeled by applying the

Fourier transform properties of the lens. The two images must both be considered when designing a Kohler illumination lens system. In the Köhler illumination schematic in Figure 8, the optical elements are separated by the focal length *f* of the lenses, and therefore the final image can be determined by utilizing the Fourier transform.

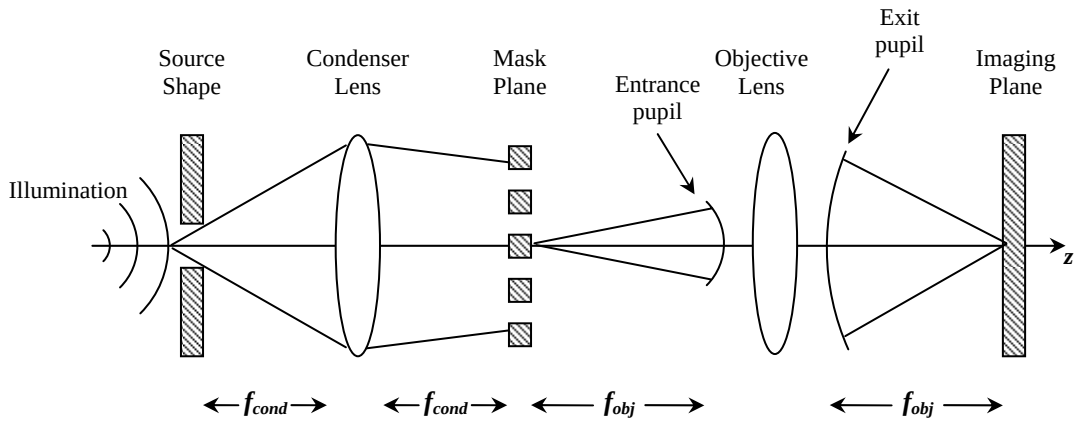

Figure 8. Conventional projection lithography utilizing Köhler illumination. The source and mask images are simultaneously passed through the imaging system.

Light is first passed through an aperture with a source shape function given by *s(x,y)* and is then propagated to the condenser lens. The Fourier transform of the source function $S\left(\frac{x}{\lambda f_{cond}}, \frac{y}{\lambda f_{cond}}\right)$ is found at the back focal plane of the condenser lens and is then multiplied by the reticle function *m(x,y)*. In the case of Figure 8, *m(x,y)* is a binary transmission mask. The field $S\left(\frac{x}{\lambda f_{cond}}, \frac{y}{\lambda f_{cond}}\right) \cdot m(x, y)$ is propagated another focal length to the entrance pupil of the projection system. In the pupil plane of the objective lens the field distribution becomes $s(-x,-y) * M\left(\frac{x}{\lambda f_{obj}}, \frac{y}{\lambda f_{obj}}\right)$, where the symbol "*"

denotes a convolution operation. The field is finally propagated through the last element of the objective lens spanning an additional focal length to the image plane where the distribution is $S\left(-\frac{x}{\lambda f_{obj}},-\frac{y}{\lambda f_{obj}}\right)\cdot m(-x,-y)$.

2.4 Imaging system impulse response

The Dirac delta or impulse function $\delta(x,y)$ is a useful mathematical construction for modeling point sources in imaging systems; it has infinitesimal area and finite volume. If the field distribution in the entrance pupil of the objective lens is a pair of Dirac delta functions symmetrically placed about the origin, the field amplitude at the image plane is the Fourier transform of this pair, which evaluates to a cosine with frequency determined by the position of the original delta functions relative to the axis of symmetry. This situation is common in projection lithography, where it represents the minimum number of frequency components required to form a usable image. A direct correlation can then be made to two-beam interference, where the wavefronts of two point sources interfere at the surface of the photosensitive substrate. The response of a system to the Dirac delta function, or impulse function, is the impulse response of the system.

To derive the effects of illumination coherence on an imaging system limited by diffraction, the impulse response for the system will be determined by applying the treatment set forth by Goodman [2]. Diffraction-limited imaging systems are defined by

the best possible reproduction of a point source through the conversion of a diverging spherical wave at the entrance pupil to a converging spherical wave at the exit pupil. The entrance and exit pupils of an imaging system are defined by the images of the internal limiting aperture in object space and image space, respectively. The spatial limit introduced to a wavefront by this aperture is the source of diffraction.

The impulse response of an imaging system can be derived based on the earlier discussion of the propagation of light through projection optics. Light from a point source $\delta(x_o, y_o)$ propagates over a distance z_1 to a series of lenses whose total impact on the propagating wavefront can be described by the application of negative quadratic phase. The outcome of the propagation is the Fraunhofer diffraction pattern of the point source:

$$\psi_{lens}(x_1, y_1) = \frac{1}{i\lambda z_1} \exp\left[\frac{i\pi}{\lambda z_1}\left[(x_1 - x_o)^2 + (y_1 - y_o)^2\right]\right] \qquad (2.22)$$

The electromagnetic field distribution then encounters the lens system with focal length *f* and the distribution after passing through the system is:

$$\psi'_{lens}(x_1, y_1) = \psi_{lens}(x_1, y_1) P(x_1, y_1) \exp\left[-\frac{i\pi}{\lambda f}\left(x_1^2 + y_1^2\right)\right] \qquad (2.23)$$

The distribution is finally propagated over distance z_2 to the imaging plane where the final result is the impulse response function *h*:

$$h(x_2, y_2; x_o, y_o) = \frac{1}{i\lambda z_2} \int\int_{-\infty}^{\infty} \psi'_{lens}(x_1, y_1) \cdot \exp\left[-\frac{i\pi}{\lambda z_2} \left[(x_2 - x_1)^2 + (y_2 - y_1)^2 \right] \right] dx_1 dy_1 \tag{2.24}$$

Substitution of equations (2.22) and (2.23) into equation (2.24) will yield a complete but rather cluttered expression for the impulse response of an imaging system.

$$h(x_2, y_2; x_o, y_o) = \frac{1}{\lambda^2 z_1 z_2} \exp\left[\frac{i\pi}{\lambda z_2} \left(x_2^2 + y_2^2 \right) \right] \exp\left[\frac{i\pi}{\lambda z_1} \left(x_o^2 + y_o^2 \right) \right] \cdot \int\int_{-\infty}^{\infty} P(x_1, y_1) \exp\left[\frac{i\pi}{\lambda} \left(\frac{1}{z_1} + \frac{1}{z_2} - \frac{1}{f} \right) \left(x_1^2 + y_1^2 \right) \right] \cdot \exp\left[-\frac{i\pi}{\lambda} \left[\left(\frac{x_o}{z_1} - \frac{x_2}{z_2} \right) x_1 + \left(\frac{y_o}{z_1} - \frac{y_2}{z_2} \right) y_1 \right] \right] dx_1 dy_1 \tag{2.25}$$

A number of key assumptions are implemented to simplify equation (2.25) through the elimination of quadratic phase factors. The first assumption that will be utilized is the lens law of geometric optics, where an imaging condition can only be satisfied provided that:

$$\frac{1}{z_1} + \frac{1}{z_2} - \frac{1}{f} = 0$$

This eliminates one of the quadratic phase terms within the integrand. The two quadratic phase terms preceding the integrand will be ignored under the assumption that the phase of each quadratic changes by a fraction of a radian over the entire wavefront. This assumption is necessary to avoid any unacceptable blur in the image due to defocus. The

remaining terms can be cast into a form representing the Fraunhofer diffraction pattern of the diffracting aperture, or put more simply the Fourier transform of $P(x,y)$, by defining the system magnification by $M = -z_2/z_1$.

2.5 Illumination coherence

Coherence is an important factor to consider when evaluating the effects of an optical system on a field distribution and the measurable intensity. The subject of illumination coherence is considered for polychromatic narrowband sources and therefore the field distribution must include a time-varying phasor to account for temporal, as well as spatial, variations. If the amplitude of the time-varying phasors varies while the phase difference remains constant, or is perfectly correlated, then the illumination is considered to be spatially *coherent*. If the phasor amplitudes vary in a completely uncorrelated fashion then the illumination is spatially *incoherent*.

The field distribution of the image is given as the convolution of the generalized impulse response of the system with the representation of the object that includes the time-varying phasor dependence:

$$\psi_{img}(x_i, y_i; t) = \int_{-\infty}^{\infty}\int h(x_i - x_o, y_i - y_o)\cdot\psi_{obj}(x_o, y_o; t-\tau)\,dx_o dy_o \tag{2.26}$$

The variable τ is included to account for the time difference in traveling from the object (x_o, y_o) to the image plane (x_i, y_i). The intensity of the final image is found by

evaluating the time average of the squared magnitude of the field distribution in equation (2.26). The spatial integral and temporal average may be interchanged when calculating the intensity giving:

$$I_i\left(x_i, y_i\right) = \int_{-\infty}^{\infty}\int dx_{o1}dy_{o1}\int_{-\infty}^{\infty}\int dx_{o2}dy_{o2}h\left(x_i - x_{o1}, y_i - y_{o1}\right)h^*\left(x_i - x_{o2}, y_i - y_{o2}\right) \cdot\left\langle \psi\left(x_{o1}, y_{o1}; t-\tau_1\right)\psi^*\left(x_{o2}, y_{o2}; t-\tau_2\right)\right\rangle \tag{2.27}$$

The temporal average $\langle\ \rangle$ in equation (2.27) is called the *mutual intensity* $J\left(x_{o1}, y_{o1}; x_{o2}, y_{o2}\right)$, which is the level of correlation between two object points on an illumination source. For coherent illumination, the time-varying phasors of the source vary in a completely correlated fashion, hence the mutual intensity function will take the following form:

$$J\left(x_{o1}, y_{o1}; x_{o2}, y_{o2}\right) = \psi\left(x_{o1}, y_{o1}\right)\psi^*\left(x_{o2}, y_{o2}\right) \tag{2.28}$$

The intensity is then just the squared magnitude of the convolution of the illuminated object with the impulse response of the system (2.29), which was found to be the Fourier transform of the pupil function $P\left(\xi, \eta\right)$. Imaging systems with coherent illumination are therefore linear in complex amplitude.

$$I_i\left(x_i, y_i\right) = \left|\int_{-\infty}^{\infty}\int dx_o dy_o h\left(x_i - x_o, y_i - y_o\right)\psi\left(x_o, y_o\right)\right|^2 \tag{2.29}$$

The *amplitude transfer function* of a coherent system is the Fourier transform of the impulse response. The amplitude transfer function is therefore $H\left(\lambda z_i \xi, \lambda z_i \eta\right) = P\left(\lambda z_i \xi, \lambda z_i \eta\right)$, neglecting the scaling constants.

Illumination that is completely incoherent will have phasor amplitudes that vary independently of one another and coherency will be constrained to very small regions. This characteristic is represented in the mutual coherence function for incoherent illumination:

$$J\left(x_{o1}, y_{o1}; x_{o2}, y_{o2}\right) = K \cdot I_o\left(x_{o1}, y_{o1}\right) \delta\left(x_{o1} - x_{o2}, y_{o1} - y_{o2}\right) \tag{2.30}$$

by way of the delta function. *K* is a proportionality constant. From the following:

$$I_i\left(x_i, y_i\right) = K \cdot \int_{-\infty}^{\infty} \int dx_o dy_o \left|h\left(x_i - x_o, y_i - y_o\right)\right|^2 I_o\left(x_o, y_o\right) \tag{2.31}$$

it can then be ascertained that incoherent illumination is linear in intensity. The incoherent OTF (Optical Transfer Function) is the Fourier transform of the incoherent impulse response $\left|h\left(x_o, y_o\right)\right|^2$, and therefore is the autocorrelation of the of the pupil function:

$$\mathcal{H}\left(\xi, \eta\right) = F.T.\left(\left|h\left(x_o, y_o\right)\right|^2\right) = P\left(\lambda z \xi, \lambda z \eta\right) \bigstar P\left(\lambda z \xi, \lambda z \eta\right) \tag{2.32}$$

2.6 Defocus aberration and the OTF

Aberrations are defined as deviations from ideal imaging conditions. The ideal conditions were described earlier in the Fourier optics treatment of a diffraction-limited imaging system. Aberrations are inherent in optics due to lens defects such as surface roughness, non-uniform glass distribution and inaccurate lens thicknesses, to name a few. A wavefront entering an aberrated imaging system will experience a change in phase that is not consistent with the phase-shift predicted by Fourier analysis. The aberration-induced phaseshift is highly dependent on the position of the wavefront within the lens pupil. It can be mathematically described by including both amplitude and phase modulations, respectively $P_{ideal}(r,\theta)$ and $W(r,\theta)$, in the description of a circular pupil function [1, 2]:

$$P(r,\theta) = P_{ideal}(r,\theta)\exp\left[i\frac{2\pi}{\lambda}W(r,\theta)\right] \qquad \begin{array}{ll} P_{ideal}(r,\theta)=0 & r>1 \\ P_{ideal}(r,\theta)=1 & r<1 \end{array} \tag{2.33}$$

Defocus is one of the most common aberrations in imaging systems and can be described by including the appropriate phase-shift $W(r,\theta)$ in the pupil function. The primary cause of defocus in projection imaging systems is the misshaping of the wavefront curvature by the lens due to phase errors in such a way that when the wavefront exits the lens the wavefront is focused at a plane other than the ideal recording plane. However, defocus may also occur in the presence of ideal wavefront curvature if the image is not measured at the ideal recording plane.

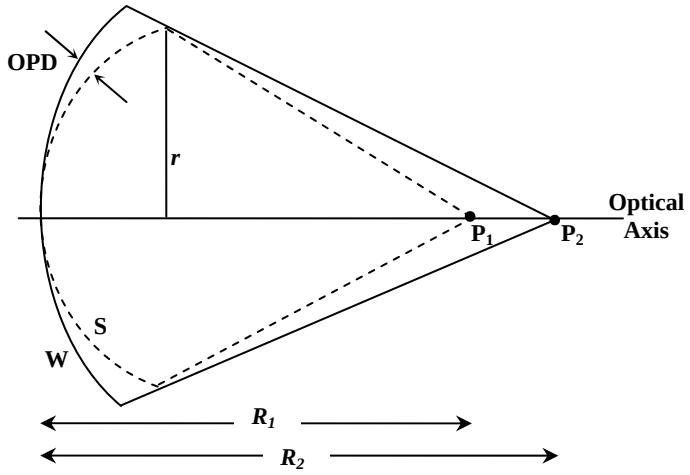

Figure 9. Optical path difference (OPD) between two converging wavefronts W (defocused) and S (reference sphere) that pass through the center of the objective lens exit pupil. Wavefront W has radius R_1 and is centered at P_1, while wavefront S has radius R_2 and is centered at P_2. The OPD is significantly exaggerated for visualization.

A spherical wavefront S with a center of curvature P_1 and radius R_1 is depicted as a dashed line in Figure 9. The wavefront W with a center of curvature P_2 and radius R_2 is shown as a solid line. The difference between them is an optical path deviation (or sag) given by the product of the imaging medium refractive index n with the geometrical path length difference at a height r above the optical axis. The path length error is mathematically represented by:

$$W(r) = \frac{n}{2}\left(\frac{1}{R_1} - \frac{1}{R_2}\right) r^2 \tag{2.34}$$

where the θ dependence is dropped due to the rotational symmetry of defocus. Note that the aberration is proportional to r^2, the normalized radius in the pupil. The path length error expressed in equation (2.34) can be related to the longitudinal defocus ΔR (defocus measured along the optical axis) by defining $R_1 \cong R_2 = R$ and $\Delta R = R_2 - R_1$ [4]:

$$W(r) = \frac{n}{2}\left(\frac{\Delta R}{R^2}\right) r^2 \qquad or \qquad W(r) = \left(\frac{n \cdot \Delta R \cdot NA^2}{2}\right) r^2 \tag{2.35}$$

The second expression in equation (2.35) is suitable for circular pupils with a numerical aperture given by *NA*. The peak value of the defocus aberration is evaluated at the edge of the pupil ($r = 1$):

$$A_d = \frac{n \cdot \Delta R \cdot NA^2}{2} \tag{2.36}$$

As seen earlier, the impulse response or Point Spread Function (PSF), of a coherent system is proportional to the Fourier transform of the pupil function. To account for a defocus aberration in the objective lens, the induced phase error in equation (2.35) must be lumped into the generalized pupil function in equation (2.33) when performing the Fourier transform. Consequently, the amplitude transfer function is simply the aforementioned generalized pupil function after appropriate scaling. The resolution limit for coherent imaging systems is not impacted by the presence of aberrations, though phase distortions are introduced. The aberrated PSF for incoherent systems is the squared magnitude of the coherent PSF that includes the appropriate phase errors. The calculations for aberrant incoherent imaging systems are much more complex for this reason. The existence of defocus will decrease the contrast of any spatial frequency components that exist within the resolution limit of the OTF and the phenomenon of contrast reversal will occur when contrast reduction results in a negative OTF for certain frequencies.

2.7 Defocus in partially coherent systems

The partial coherence of the illumination may be used by lithographers to engineer the OTF of an imaging system to maintain high modulation over a pre-determined set of spatial frequencies. The projection lithography systems examined throughout this work utilize partially coherent illumination primarily to obtain better modulation than incoherent illumination while still exceeding the coherent resolution limit. The groundwork for this discussion on partial coherence has been generalized from treatments by Kintner [5], Subramanian [6], Lin [7] and most notably Hopkins [8, 9].

Hopkins' theory of image formation with partially coherent light assumes that the area element $d\sigma$ of a quasi-monochromatic source illuminates an object with a complex amplitude disturbance $\psi_{src}(x_1, y_1)$. The complex transmission of the object is given by $f(x_1, y_1)$ and the response of this interaction at a point (x, y) in the image plane is a complex amplitude denoted by $h(x, y)$. The total amplitude in the image plane is found by integrating over the source element $d\sigma = dx_1 dy_1$:

$$\int_{src_1} \psi_{src}(x_1, y_1)\, f(x_1, y_1)\, h(x - x_1, y - y_1)\, dx_1 dy_1 \tag{2.37}$$

The intensity due to $d\sigma$ is the product of the complex amplitude in equation (2.37) with its complex conjugate:

$$dI = \left\langle \int_{src_1} \psi_{src}\left(x_1, y_1\right) f\left(x_1, y_1\right) h\left(x - x_1, y - y_1\right) dx_1 dy_1 \right.$$
$$\left. \cdot \int_{src_2} \psi^*_{src}\left(x_2, y_2\right) f^*\left(x_2, y_2\right) h^*\left(x - x_2, y - y_2\right) dx_2 dy_2 \right\rangle d\sigma \tag{2.38}$$

The total intensity is obtained by integrating over the entire source represented by Σ:

$$I = \int_{src_1}\int_{src_2} \left\langle \int_{\Sigma} \psi_{src}\left(x_1, y_1\right)\psi^*_{src}\left(x_2, y_2\right) d\sigma \right\rangle f\left(x_1, y_1\right) f^*\left(x_2, y_2\right)$$
$$\cdot h\left(x - x_1, y - y_1\right) h^*\left(x - x_2, y - y_2\right) dx_2 dy_2 dx_1 dy_1$$
$$= \int_{src_1}\int_{src_2} J\left(x_1, y_1; x_2, y_2\right) f\left(x_1, y_1\right) f^*\left(x_2, y_2\right) \tag{2.39}$$
$$\cdot h\left(x - x_1, y - y_1\right) h^*\left(x - x_2, y - y_2\right) dx_2 dy_2 dx_1 dy_1$$

where all terms may be excluded with the exception of ψ and its complex conjugate. $J\left(x_1, y_1; x_2, y_2\right)$ is the mutual intensity function and $h\left(x_i, y_i\right)$ is the coherent impulse response, which were described earlier in the discussion on illumination coherence.

Partially coherent fields in projection imaging systems are highly nonlinear and therefore the calculation of the image intensity utilizing equation (2.39) can become quite complicated. To simplify the analysis, the functions are expressed in terms of the dimensionless coordinates:

$$x = x' \frac{NA_{obj}}{\lambda} \qquad y = y' \frac{NA_{obj}}{\lambda} \tag{2.40}$$

where *x'* and *y'* are the geometric coordinates, NA_{obj} is the numerical aperture of the objective lens and λ is the mean wavelength. Hopkins' intensity relation will be examined in the spatial frequency domain by taking the Fourier transform of equation (2.39):

$$I(\xi,\eta) = \int_{-\infty}^{\infty}\int T(\xi+\xi_1,\eta+\eta_1;\xi_1,\eta_1)F(\xi+\xi_1,\eta+\eta_1)F^*(\xi_1,\eta_1)d\xi_1 d\eta_1 \tag{2.41}$$

where $FT\left[f(x,y)\right] = F(\xi,\eta)$ and $T(\xi,\eta)$ is the "transmission cross coefficient" (TCC) that characterizes the elements of the optical system:

$$T(\xi_1,\eta_1;\xi_2,\eta_2) = \int_{-\infty}^{\infty}\int \tilde{J}(\xi,\eta)H(\xi+\xi_1,\eta+\eta_1)H^*(\xi+\xi_2,\eta+\eta_2)d\xi d\eta \tag{2.42}$$

where $\tilde{J}(\xi,\eta)$ is the Fourier transform of the mutual intensity function (effectively the source aperture) and $FT\left[h(x,y)\right] = H(\xi,\eta)$ is the coherent OTF, or the complex pupil function $P(\xi,\eta)$ of the objective lens. The TCC is valid for the special cases of coherent or incoherent illumination where equation (2.42) reduces to the squared magnitude of the pupil function and the incoherent OTF, respectively. In an imaging system with circular optical elements, the TCC is proportional to the area of intersection of three uniform circles, the source aperture and the shifted objective pupils, as shown in Figure 10 [5]:

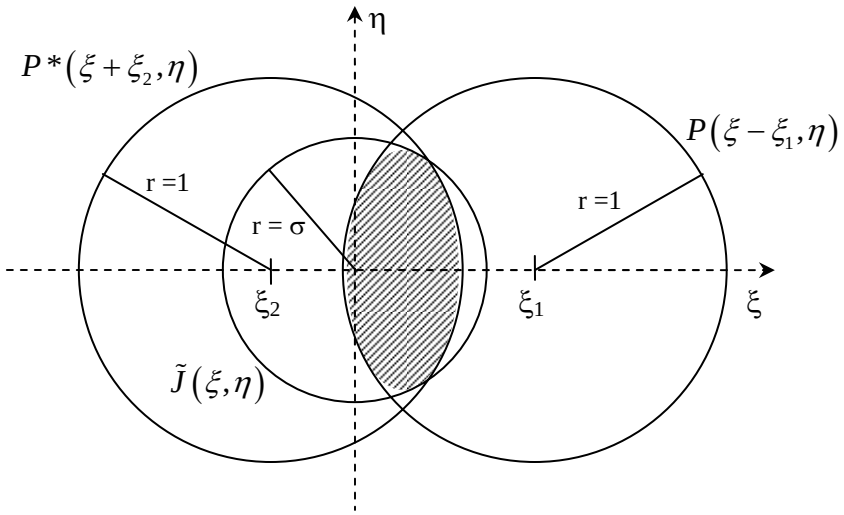

Figure 10. Three intersecting circles, which include the complex pupil function, its complex conjugate and the source aperture that enables the calculation of the TCC. The normalized pupil functions have a radius of unity, while the radius of the source aperture is the ratio of the condenser *NA* to the objective *NA*, which is termed σ.

If the radius of the source aperture is assumed to be smaller than the pupil, then all radii may be normalized to the pupil and the source aperture radius will be some fraction of the pupil. The radius of the pupil is defined by the numerical aperture of the objective lens NA_{obj}. The radius of the normalized source aperture is taken as the ratio of the numerical aperture of the condenser to that of the objective and is called sigma, $NA_{cond} \big/ NA_{obj} = \sigma < 1$. The intensity within all pupil functions in Figure 10 is assumed to be uniformly distributed provided that the pupil is unaberrated, however if defocus is present additional phase variations must be incorporated into the TCC computation. According to equation (2.35) imaging calculations for partially coherent systems with

defocus can be quite cumbersome and therefore these calculations will be performed utilizing a industry standard aerial image simulator.

3 Synthesis of projection lithography

3.1 Two-beam interference

The principle of superposition can be utilized to derive the intensity distribution resulting from the interference of two beams of light. The electric field distribution $\vec{E}$ at a point in space is found by summing the component electric fields $\vec{E}_n$ of each source: $\vec{E}_1$ and $\vec{E}_2$. Assuming both beams are monochromatic plane waves with the same frequency, then the complex amplitude of each wave can be represented by:

$$\vec{E}_1 = \vec{E}_{01}\exp\left[i\left(\vec{k}_1\cdot\vec{r}+\phi_1\right)\right] \qquad \vec{E}_2 = \vec{E}_{02}\exp\left[i\left(\vec{k}_2\cdot\vec{r}+\phi_2\right)\right] \tag{2.43}$$

where $\vec{k}_1$ and $\vec{k}_2$ are the wave propagation vectors, ϕ_1 and ϕ_2 are the initial phase terms, and $\vec{r} = x\hat{i} + y\hat{j} + z\hat{k}$ is a position vector [10, 11]. The intensity (or irradiance) is the measurable quantity:

$$\begin{aligned}\left\langle\left|\vec{E}\right|^2\right\rangle &= \left\langle\vec{E}_1+\vec{E}_2\right\rangle\cdot\left\langle\vec{E}_1^*+\vec{E}_2^*\right\rangle \\ \left\langle\left|\vec{E}\right|^2\right\rangle &= \left\langle\left|\vec{E}_1\right|^2\right\rangle+\left\langle\left|\vec{E}_2\right|^2\right\rangle+2\left\langle\vec{E}_1\cdot\vec{E}_2^*\right\rangle\end{aligned} \tag{2.44}$$

where $\langle\ \rangle$ denotes the average over the time interval $2T$:

$$\left\langle f(x)\right\rangle = \frac{1}{2T}\int_{-T}^{T} f(x)dt \tag{2.45}$$

Since the intensity of a wave is proportional to the square of the electric field, then $\left\langle \vec{E}^2 \right\rangle$ $\propto I$. The intensity distribution of the interference pattern is:

$$I = I_1 + I_2 + 2\left\langle \vec{E}_1 \cdot \vec{E}_2^* \right\rangle \tag{2.46}$$

where I_1 and I_2 represent the intensities of the individual waves. $\vec{E}_1 \cdot \vec{E}_2$ is the *mutual coherence* and vanishes if the light is *incoherent* and must be non-zero for the waves to interfere. For two orthogonal electric field vectors, the dot product is zero and there is no interference; therefore only the parallel components of the electric field vectors $\vec{E}_1$ and $\vec{E}_2$ interfere. This description is valid if the interfering medium is isotropic and free of electric charge. The two electric field vectors are said to be *coherent* if the phase relation between the two beams is constant. The total irradiance may be written as:

$$I = I_1 + I_2 + 2\sqrt{I_1 I_2}\cos\delta \tag{2.47}$$

where δ is the *phase difference* between the two interfering beams [10, 11]. The phase difference δ for beams with the same frequency can be described by the difference in propagation path, as well as the differences due to the initial phase of each oscillator, equation (2.43). If the two beams have the same amplitude, the resulting intensity may be expressed as:

$$I = 2I_1\left(1+\cos\delta\right) \;=\; 4I_1\cos^2\left(\frac{\delta}{2}\right) \tag{2.48}$$

when the well-known trigonometric identity has been used.

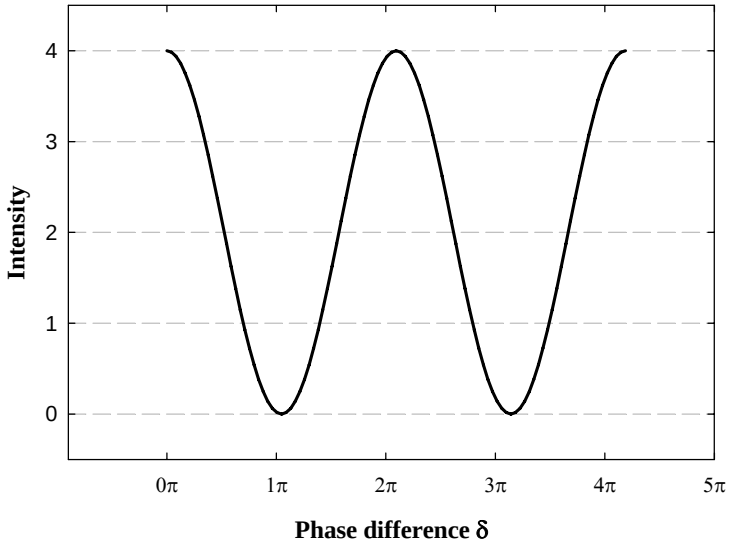

Figure 11. Intensity distribution as a function of phase difference between two interfering electromagnetic waves.

An example of interference between two monochromatic beams impinging on a substrate at an angle θ_2 with the plane of incidence in the *x-y* plane is illustrated in Figure 12. The dot products of the propagation vectors with the position vector $\vec{r}$ for each beam is defined as $\vec{k}_1 \cdot \vec{r} = \frac{2\pi}{\lambda/n}\left(x\cos\theta_1 - y\sin\theta_1\right)$ and $\vec{k}_2 \cdot \vec{r} = \frac{2\pi}{\lambda/n}\left(-x\cos\theta_1 - y\sin\theta_1\right)$, where n is the refractive index of the surrounding medium. If the initial phases of each beam are assumed to be equal, then the phase difference δ in equation (2.48) can be determined by subtracting the aforementioned dot products.

$$\begin{aligned}\vec{k}_1 \cdot \vec{r} - \vec{k}_2 \cdot \vec{r} &= \frac{2\pi}{\lambda/n}\left[\left(x\cos\theta_1 - y\sin\theta_1\right) - \left(-x\cos\theta_1 - y\sin\theta_1\right)\right] \\ &= \frac{4\pi}{\lambda/n}\, x\cos\theta_1\end{aligned} \tag{2.49}$$

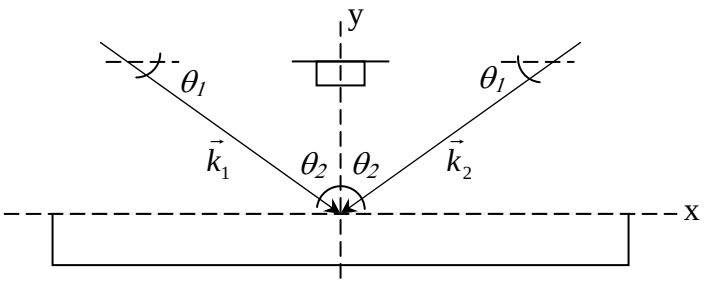

Figure 12. Interference of two light beams at an angle θ_2 with the substrate normal and with propagation vectors $\vec{k}_1$ and $\vec{k}_2$.

The constructive interference nodes for the interfering beams in Figure 12 will occur at $\delta = 2\pi m$ (where possible values of *m=0, ±1, ±2, . . .*). This representation of δ is then equated to the phase difference in equation (2.49) so that the locations along the *x*-axis where constructive interference occurs may be ascertained.

$$\frac{4\pi n}{\lambda} x \cos\theta_1 = 2\pi m$$
$$x = \frac{m\lambda}{2n\cos\theta_1} \tag{2.50}$$

$$P = \left.\frac{m\lambda}{2n\cos\theta_1}\right|_{m=2} - \left.\frac{m\lambda}{2n\cos\theta_1}\right|_{m=1} = \frac{\lambda}{2n\cos\theta_1} \tag{2.51}$$

The pitch (spatial period) of the interference pattern is defined by the distance *x* between successive constructive interference nodes in equation (2.51). Figure 12 reveals that $\cos\theta_1 = \sin\theta_2$, where θ_2 is acceptance angle. This term can be expressed in a form similar to the *NA* of the Rayleigh criterion for resolution seen earlier, where the effective

numerical aperture is $NA_{eff} = n\sin\theta_2$ when appropriately scaled by the refractive index of the interfering medium. Therefore, the pitch is:

$$P = \frac{\lambda}{2n\sin\theta_2} \text{ or } \frac{\lambda}{2NA_{eff}} \tag{2.52}$$

3.2 Interferometric lithography

Two-beam interference may be used in the patterning technique known as interferometric lithography (IL). IL is based on the interference of two mutually coherent light beams of wavelength λ at the surface of a photosensitive substrate. The interfering beams produce a high-contrast sinusoidal intensity pattern that exposes a periodic array of lines and spaces in the photosensitive material. The contrast of these patterns is maintained over a large depth of focus, of the order of centimeters that may be considered infinite. The depth of focus is limited by any unmatched path lengths in each arm of the interferometer that are induced by variations in the beam diameter, beam intensity profile and the angle of intersection [12].

IL systems are valuable research tools for the study of resist chemistries and properties, as well as in the evaluation of new wavelengths and the recently emerging liquid immersion lithography (LIL) technology. In addition, IL may be implemented with minimum complexity, since there is limited use of masks and refractive components that may induce aberrations in the propagating wavefronts [13].

The minimum resolvable line width in an IL system decreases as the angle of incidence increases. The minimum period that can be achieved is $\lambda/2n$ when the waves interference angle approaches π, which allows for resolution far exceeding a quarter-wavelength when an immersion medium is introduced. This is possible since interferometric lithography may be described as having a k_1 of 0.25 when considering the half-pitch of the period given in equation (2.52). Simple adjustments may be made to the angle of interference that will allow a wide range of pitches to be studied.

Significant control over aerial image modulation is also possible by changing the balancing of the intensities of the interferometer arms. Attenuation of one of the two interfering beams in an interferometric lithography system enables the synthesis of other attributes of projection lithography, such as the modulation due to defocus. The intensity imbalance causes only a portion of the un-attenuated beam to interfere with the other leaving behind excess illumination that resembles the intensity bias typically attributed to the 0^{th} diffraction order. This intensity bias can be utilized to induce demodulation in the resulting intensity profile of the interfering beams, which can be correlated to a similar demodulation effect that occurs when defocus is introduced to a projection lithography system. The ability to synthesize this effect through the use of interferometric lithography will be studied throughout the course of this work.

3.3 Modulation in two-beam interference

The expression for the resulting intensity from two-beam interference in equation (2.48) assumes unit modulation. To account for levels of modulation less than unity, the modulation factor *m* is introduced to equation (2.48):

$$I = \frac{1}{2} + \frac{1}{2} m \cos\delta \tag{2.53}$$

where $0 \le m \le 1$. The maximum intensity in equation (2.53) has been normalized. The modulation term *m* arises from a number of factors including illumination coherence and polarization. Imbalanced intensities between the two interfering beams also contributes to the level of modulation, however this effect will be discussed in detail in the next section.

The modulation term may be broken down into the product of the individual contributions such that:

$$\begin{aligned} m &= \left|\gamma_{12}\right| a_P a_I \\ I &= \frac{1}{2} + \frac{1}{2}\left|\gamma_{12}\right| a_P a_I \cos\delta \end{aligned} \tag{2.54}$$

where $\left|\gamma_{12}\right|$ is the contribution due to coherence, a_P is the polarization contribution and a_I is the modulation due to intensity imbalance.

A more detailed evaluation of the dot product in equation (2.46) is required to derive the impact of polarization on the modulation of the two-beam interference intensity pattern. When considering polarization, the dot product will initially reduce to:

$$\left\langle \vec{E}_1 \cdot \vec{E}_2^* \right\rangle = \left\langle \vec{E}_{01} \cdot \vec{E}_{02}^* \right\rangle \cos\delta \tag{2.55}$$

where δ is the phase difference between the two interfering beams. The electric field vectors in the time average may then be broken down into their TE and TM polarization components:

$$\begin{aligned} \vec{E}_{01} \cdot \vec{E}_{02}^* &= \left(\vec{E}_{01\,\mathrm{TM}} + \vec{E}_{01\,\mathrm{TE}} \right) \cdot \left(\vec{E}_{02\,\mathrm{TM}}^* + \vec{E}_{02\,\mathrm{TE}}^* \right) \\ \vec{E}_{01} \cdot \vec{E}_{02}^* &= \vec{E}_{01\,\mathrm{TM}} \cdot \vec{E}_{02\,\mathrm{TM}}^* + \vec{E}_{01\,\mathrm{TE}} \cdot \vec{E}_{02\,\mathrm{TE}}^* \end{aligned} \tag{2.56}$$

The cross terms in the dot product of equation (2.56) vanish since the TE and TM vectors are orthogonal. The remaining dot products may be simplified by examining Figure 13.

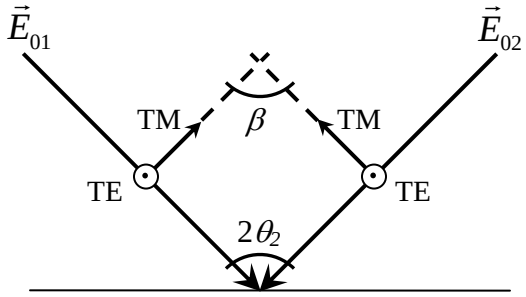

Figure 13. Two-beam interference with each interfering beam broken down into its TE and TM components.

Regardless of the angle of interference $2\theta_2$, the TE components of the interfering beams (polarization out of the page in Figure 13) will always be parallel. Therefore, the polarization contribution to modulation a_P is unity and the dot product in equation (2.56) reduces to $E_{01\,\mathrm{TE}} \cdot E_{02\,\mathrm{TE}}^*$ for TE polarized interference. However, the only occurrence

where the interfering TM components (polarization in the plane of the page) will produce a_P = 1 is when the two beams $\vec{E}_{01}$ and $\vec{E}_{02}$ are parallel or anti-parallel; otherwise a_P will fall off as the angle β between the two TM components increases since:

$$\vec{E}_{01\,\mathrm{TM}} \cdot \vec{E}^{*}_{02\,\mathrm{TM}} = \left(E_{01\,\mathrm{TM}} \cdot E^{*}_{02\,\mathrm{TM}} \right) \cos\beta \tag{2.57}$$

where β is the angle shown in Figure 13. Equation (2.55) may now be rewritten to include the modulation due to polarization as:

$$\left\langle \vec{E}_1 \cdot \vec{E}^{*}_2 \right\rangle = \left\langle E_{01\,\mathrm{TE}} \cdot E^{*}_{02\,\mathrm{TE}} \right\rangle \cos\delta + \left\langle E_{01\,\mathrm{TM}} \cdot E^{*}_{02\,\mathrm{TM}} \right\rangle \cos\beta \cos\delta \tag{2.58}$$

The corrected expression for two-beam interference including polarization is approximated by:

$$\begin{aligned} I &= \frac{1}{2} + \frac{1}{2} a_P \cos\delta \\ \text{where } a_P &= \begin{cases} 1, \text{ TE} \\ \cos\beta, \text{ TM} \end{cases} \end{aligned} \tag{2.59}$$

TE polarized illumination will be utilized in this experiment to eliminate the reduction in modulation that is attributed to the TM component.

The coherence contribution to modulation, $\left|\gamma_{12}\right|$, is found by evaluating the two time averages in equation (2.58). This contribution depends on the coherence of the illumination source and the relative phase variations between each interfering beam. The term $\left|\gamma_{12}\right|$ is mathematically expressed as:

$$\left|\gamma_{12}\right| = \frac{\left\langle E_{01} \cdot E_{02}^{*} \right\rangle}{\left(\left\langle E_{01}^{2} \right\rangle \left\langle E_{02}^{2} \right\rangle\right)^{1/2}} \tag{2.60}$$

where the time average has been normalized to the geometric mean of the two interfering beam intensities. Therefore, the range of possible values for $\left|\gamma_{12}\right|$ is 0 to 1. Equation (2.59) may now be appended to include the coherence term:

$$\begin{aligned} I &= \frac{1}{2} + \frac{1}{2}\left|\gamma_{12}\right| a_P \cos\delta \\ \text{where } a_P &= \begin{cases} 1, \text{ TE} \\ \cos\beta, \text{ TM} \end{cases} \\ 0 \le \left|\gamma_{12}\right| &\le 1 \qquad 0 \le a_P \le 1 \end{aligned} \tag{2.61}$$

$\left|\gamma_{12}\right|$=1 for coherent illumination.

3.4 Demodulation through intensity imbalance

The aerial image that is created by interference of two mutually coherent beams may be demodulated by changing the balance of the intensity between the two beams. If two interfering beams are assumed to have the same intensity, the un-normalized aerial image distribution is given by:

$$I\left(x\right) = 2I_1\left(1 + \cos\left(Kx\right)\right) \tag{2.62}$$

where $K = 2\pi/\Lambda$ and Λ is the period of the interference pattern [14]. This relation is similar to the one developed in equation (2.48), however the phase relation here is

expressed as a function of the spatial coordinate *x*. An intensity imbalance between the interfering beams may be generated by attenuating one of the beams during exposure or by performing two independent exposures. In the latter case, an aerial image intensity distribution with 100% modulation will be created by a two-beam exposure. The second exposure will demodulate this intensity distribution by blocking one of the beams completely and allow the unobstructed beam to deliver a DC intensity bias to the original aerial image. The demodulated intensity distribution assuming TE polarization and coherent illumination is given by:

$$I\left(x\right) = 2I_1\left(1 + a_I \cos\left(Kx\right)\right) \tag{2.63}$$

where a_I is the induced level of modulation due to the intensity imbalance.

The two-pass exposure method of inducing demodulation that is described above may be mathematically visualized in terms of the delivered dose by adjusting the following intensity relation:

$$I = \underbrace{2I_1 \cdot \left(1 + \cos\left(Kx\right)\right)}_{2-Beam} + \underbrace{I_2}_{\substack{Single \\ Beam}} \tag{2.64}$$

The 2-beam exposure and the single beam exposure can be derived by taking a product of equation (2.64) with the appropriate exposure times t_1 and t_2, respectively:

$$D = D_1 + D_2 = \underbrace{2I_1 \cdot t_1 \cdot \left(1 + \cos\left(Kx\right)\right)}_{2-Beam} + \underbrace{I_2 \cdot t_2}_{\substack{Single \\ Beam}} \tag{2.65}$$

The result is the total dose *D* or total energy per incident area, where $D_n = I_n \cdot t_n$ and *n* is the exposure pass. The modulation (contrast) is the ratio of the difference to the sum of the maximum and minimum doses:

$$a_I = \frac{D_{\max} - D_{\min}}{D_{\max} + D_{\min}} = \frac{2I_1 \cdot t_1}{2I_1 \cdot t_1 + I_2 \cdot t_2} \tag{2.66}$$

If the demodulation is viewed as an imbalance over time rather than intensity, then it may be assumed that $I_1 \approx I_2$ and t_2 is some percentage *p* of t_1, giving:

$$a_I = \frac{2}{2+p} \tag{2.67}$$

The modulation a_{DF} attained from defocusing a projection lithography system is set equal to a_I to calculate the percentage *p* of time t_1 that a single-beam exposure must be conducted, rather than a two-beam exposure.

4 Simulation

The correlation between the image intensity distribution produced by a defocused projection configuration to that of an interferometric system was accomplished through the modulation, or contrast of the aerial image. Due to the complexity of simulating projection lithography with partially coherent or off-axis illumination, the aerial image simulator Prolith was utilized to extract the modulation for the projection system.

The extracted modulation is specific to the projection configuration and level of defocus input into the aerial image simulator, and is termed a_{DF}. The modulation a_{DF} is equated to a_I (the desired two-beam interference modulation) and equation (2.67) is used to calculate the percentage p of t_1 (the two-beam exposure time). This allows calculation of t_2 for a second-pass, single-beam exposure. The second-pass exposure allows the two-beam interference pattern generated during the first exposure pass to be demodulated on a level equivalent to that of the defocused projection system.

4.1 Interference model

The aerial image simulator was not designed to facilitate two-beam interference; therefore certain approximations were required to model the effect. A coherent, TE polarized illumination source was passed through a chromeless phase-shifted grating to generate the two mutually coherent beams to be interfered at the image plane. The pitch of the phase grating was determined so that the $\pm 1^{st}$ diffraction orders would be placed at

the very edge of the *NA* that would reproduce a pitch to match that of the defocused projection system being synthesized. A pupil filter was used to block one beam to appropriately emulate the single-beam exposure.

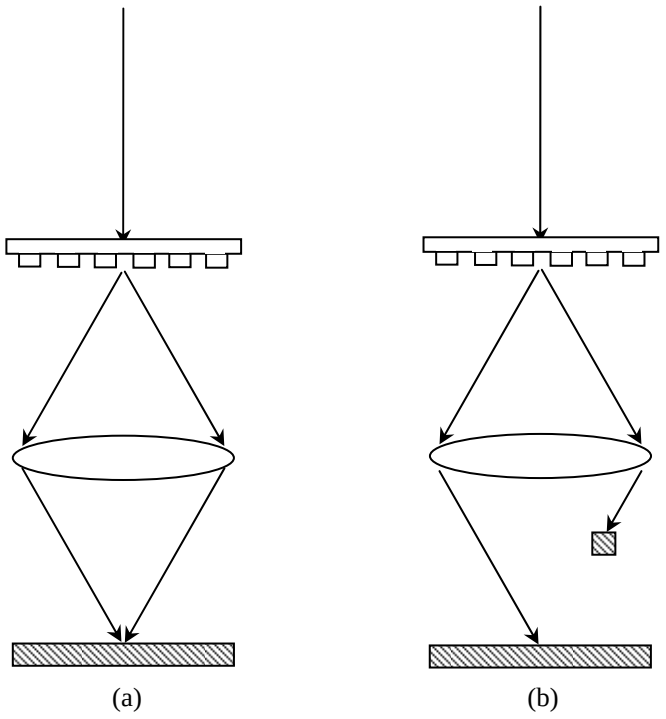

Figure 14. Diagram of the (a) two-beam first exposure pass and the (b) second pass exposure, where one beam is blocked using a pupil filter.

4.2 Simulation example

A simulation was conducted to synthesize a partially coherent projection configuration with $\sigma = 0.3$ and $NA = 0.98$ utilizing the interferometric technique. In the projection system, an illumination $\lambda = 248$ nm was passed through a 1:1 alternating

phase shift mask with a target feature size of 89 nm, assuming a k_1 of 0.35. The equivalent "*NA*" (sine of the half-angle between the two interfering beams) required in the interferometric system to reproduce 89 nm features utilizing the same wavelength is 0.70.

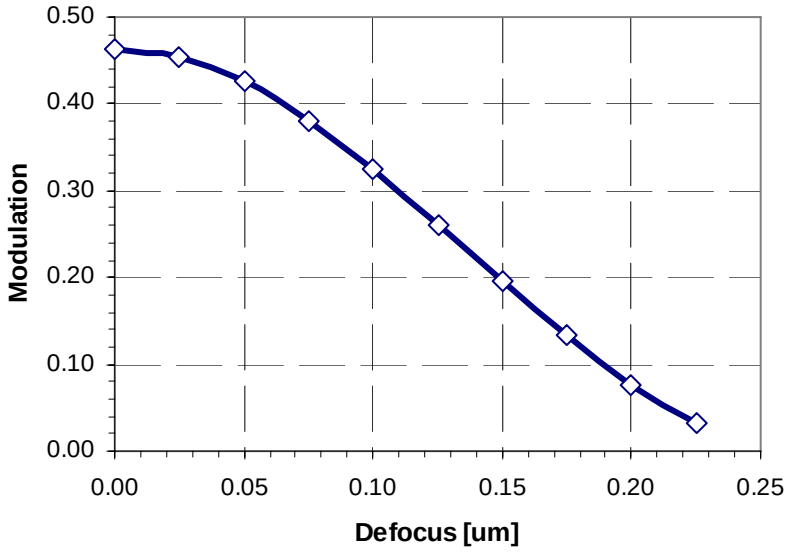

Figure 15. The resulting aerial image modulation is pictured as a function of the induced defocus in a projection system with an *NA*=0.98 and σ=0.3.

Defocus was varied in the projection system from 0 to 0.225 μm, and the aerial image modulation was determined for each focal position and plotted in Figure 15. The modulation decreases with increased exposure, which is anticipated since it is known that defocused (blurred) images are difficult to print.

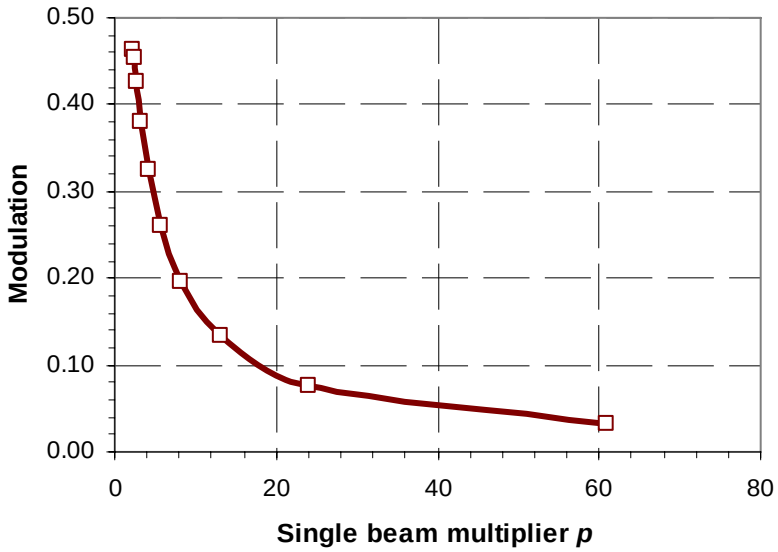

Figure 16. The attained aerial image modulation vs. the multiplier that is applied to an interferometric lithography system to reproduce that modulation.

As discussed in the previous section, the resulting modulation from defocus in the projection system was set equal to the desired two-beam interference modulation a_I (equation (2.67)) to extract the multiplier for the second-pass exposure. The multiplier may be applied to the time used for the two-beam exposure to determine the time for the single-beam exposure that will demodulate the aerial image. The modulation is plotted as a function of the calculated multiplier p in Figure 16. The modulation in Figure 16 decreases with increased single-beam exposure, as expected.

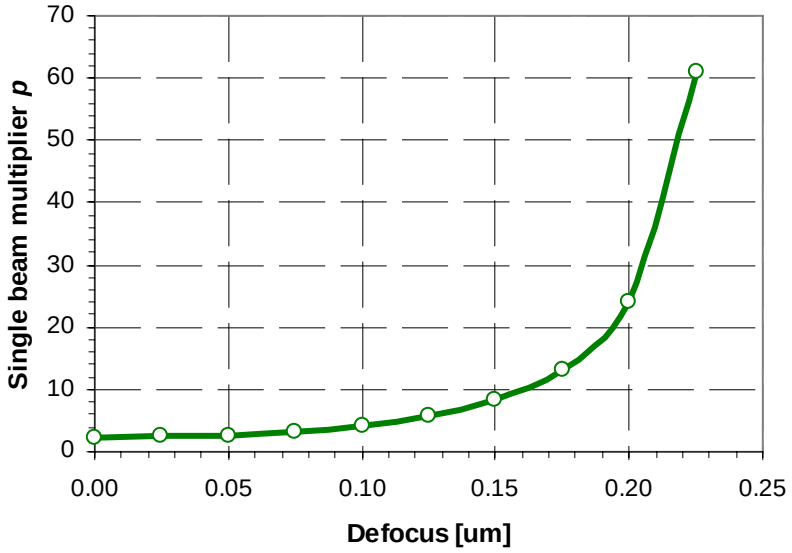

Figure 17. The required single beam multiplier necessary is plotted as a function of the level of defocus in the projection system. The two factors are related through the aerial image modulation.

If the modulations in Figure 15 and Figure 16 are set equal, the single-beam multiplier *p* may then be expressed as a function of the level of defocus in the projection system. The graph in Figure 17 is used as a lookup table for determining the appropriate amount of single-beam exposure.

4.3 Modulation Transfer Curves

A construct known as Tone Reproduction Analysis is used in negative-positive imaging systems to understand how the tone scale is modified as imaging progresses from input to output. The stages of the negative-positive system are divided into four quadrants, where adjacent quadrants share an axis. The advantage of the four-quadrant system is that it allows the designer to examine the tone transfer throughout the entire

process at once. This concept has been applied to the correlation of defocus in projection to the DC bias applied during single beam exposure in a two-beam interferometric system.

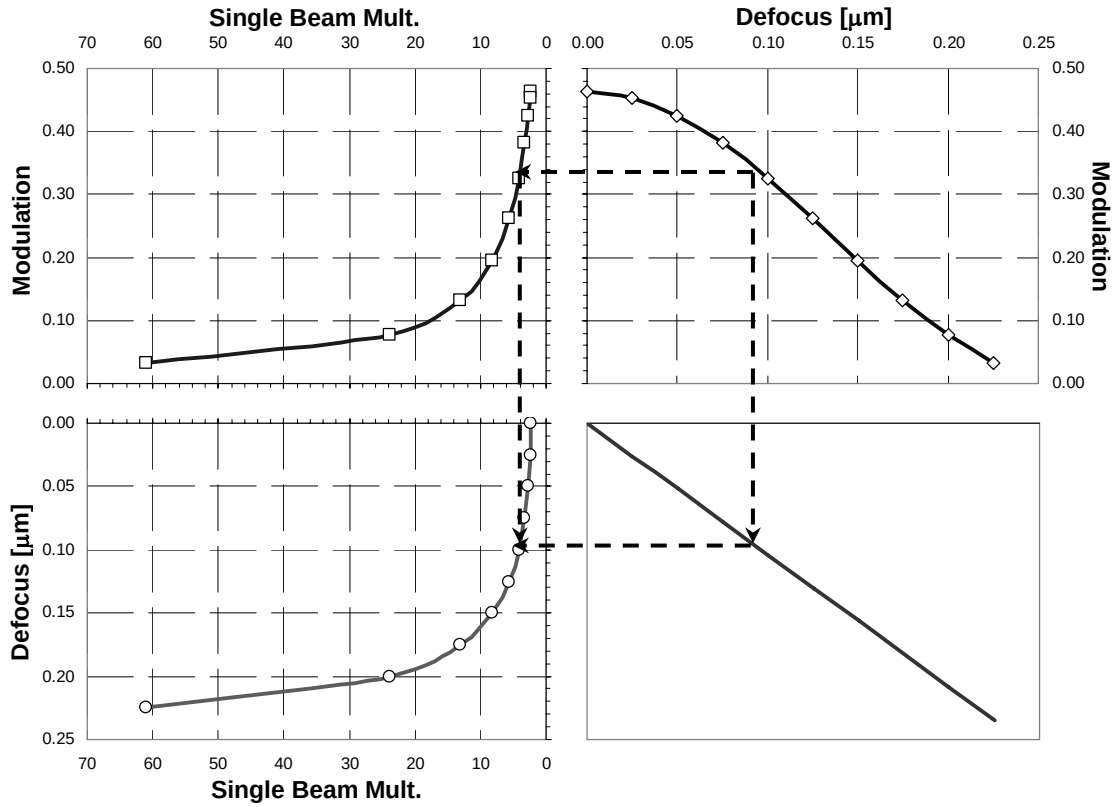

Figure 18. Modulation Transfer Curve for the synthesis of a partially coherent source configuration (σ = *0.3*) and 1:1 89nm features at a k_1 of 0.35. Defocus was varied from 0 to 225nm.

A "Modulation Transfer Curve" may be mapped out, as pictured in Figure 18, to quickly and efficiently determine the necessary single-beam exposure to synthesize a particular defocus in a projection system. A modulation is determined from a specified

defocus condition and then translated into the appropriate single-beam exposure multiplier for two-beam interference.

The first quadrant contains the resulting modulation due to an induced defocus in the projection system. The second quadrant takes that modulation and translates it into the single beam factor that will recreate the same level of modulation in a two-beam interference system. This factor is then related back to the original defocus through the defocus 1:1 relation in quadrant four and is then plotted in quadrant three.

4.4 Visual Basic module code

The following Visual Basic code is a sample of the code used to simulate the defocus condition in the projection system, as well as for the demodulation in the interferometric case.

```
' Initialize the subroutine Synthesis
Public Sub Synthesis()

   ' Define inputs for Prolith filenames
   Dim PathString As String
   Dim filename As String
   Dim intfilename As String

   ' Connecting to/Starting Prolith
   ConnectProlith

   ' Get Projection and Interferometric Prolith files
   filename = TextBox5.Text
   If filename = "" Then
     Exit Sub
   End If

   intfilename = TextBox6.Text
   If intfilename = "" Then
   Exit Sub
```

```
    End If

' Initialize variables
    Dim FocusValue As Single
    Dim FocusStop As Single
    Dim FocusStep As Single

    Dim FocusMod As Single
    Dim FocusNils As Single

    Dim SynthDose As Single
    Dim SynthMod As Single
    Dim SynthNils As Single

    Dim marker As Integer
    Dim rownum As Integer

    FocusValue = TextBox1
    FocusStop = TextBox2
    FocusStep = TextBox3

    ' Make a table to store the values for each pass through the loop
    Sheet1.Cells(1, 1).Value = "Focus"
    Sheet1.Cells(1, 2).Value = "Modulation (D)"
    Sheet1.Cells(1, 3).Value = "NILS (D)"
    Sheet1.Cells(1, 4).Value = "Second Pass Dose"
    Sheet1.Cells(1, 5).Value = "Modulation (S)"
    Sheet1.Cells(1, 6).Value = "NILS (S)"
    marker = 0

    LoadDocument filename

    Do While FocusValue < FocusStop + FocusStep

        ' Simulate Focus Condition
        RemoveAllVariables
        AddCustomInput Input_Focus, FocusValue, FocusValue, 0.1
        AddCustomOutput Output_Image_Contrast
        AddCustomOutput Output_NILS
        RunCustomSim
```

```
      Reccnt = ProlithSimulationEngine.NumResultsRecords
      For RecIndx = 0 To Reccnt - 1 Step 1

         FocusMod = ProlithSimulationEngine.GetOutput(Output_Image_Contrast,
RecIndx)
         FocusNils = ProlithSimulationEngine.GetOutput(Output_NILS, RecIndx)
         Sheet1.Cells(marker + 2, 2).Value = FocusMod
         Sheet1.Cells(marker + 2, 3).Value = FocusNils
      Next RecIndx

      Sheet1.Cells(marker + 2, 1).Value = FocusValue

      ' Step and Repeat
      marker = marker + 1
      FocusValue = FocusValue + FocusStep

   Loop

   LoadDocument intfilename
   FocusValue = TextBox1
   marker = 0

   Do While FocusValue < FocusStop + FocusStep

      ' Calculate Required Second Pass Exposure
      FocusMod = Sheet1.Cells(marker + 2, 2)
      SynthDose = 2 * (1 - FocusMod) / FocusMod
      Sheet1.Cells(marker + 2, 4).Value = SynthDose

      ' Simulate Synthesis Condition
      RemoveAllVariables
      AddCustomInput Input_Pass2_Exposure, SynthDose, SynthDose, 0.1
      AddCustomOutput Output_Image_Contrast
      AddCustomOutput Output_NILS
      RunCustomSim

      Reccnt = ProlithSimulationEngine.NumResultsRecords
      For RecIndx = 0 To Reccnt - 1 Step 1

         SynthMod = ProlithSimulationEngine.GetOutput(Output_Image_Contrast,
RecIndx)
```

```
            SynthNils = ProlithSimulationEngine.GetOutput(Output_NILS, RecIndx)
            Sheet1.Cells(marker + 2, 5).Value = SynthMod
            Sheet1.Cells(marker + 2, 6).Value = SynthNils
        Next RecIndx

        ' Step and Repeat
        marker = marker + 1
        FocusValue = FocusValue + FocusStep

    Loop

    ' Disconnecting from/Closing PROLITH
    DisconnectProlith

End Sub
```

5 Experiment

5.1 Experimental approach

Modulations of 0.3, 0.5, 0.7 and 1.0 were generated using the Smith-Talbot interferometer at NA = 0.7, which corresponds to a pitch of approximately 180 nm for 248 nm illumination. Initially, modulations of 0.3, 0.35, 0.4 and 0.45 were going to be examined, however it was difficult to discern between the modulations due to SEM inaccuracies and laser non-uniformity. The broader range of modulations proved to be more suited to the equipment used. Each modulation was considered separately when determining the appropriate exposure range and exposure increment to achieve ±30% CD variation from the half-pitch of 90 nm. The simple development threshold model [14]:

$$CD = \frac{\Lambda}{\pi} arc\cos\left(\frac{1-\frac{D_{Size}}{D}}{m}\right) \tag{4.1}$$

was evaluated to 60 and 120 nm to calculate the maximum and minimum exposure times, respectively. The terms in equation (4.1): D is the total exposure time, D_{Size} is the exposure time to create equal lines and spaces, m is the total modulation and Λ is the pitch. The D_{Size} was obtained experimentally for every wafer coated, however it was found that 2 seconds was the optimal D_{Size} in each case. The exposure time increment

was calculated by dividing the predetermined exposure range into 20 exposure times so that lower modulations would be sampled more heavily.

*All times are in units of seconds

Modulation	Minimum exposure time	Maximum exposure time	Exposure increment
0.3	1.739	2.353	0.0307
0.5	1.600	2.667	0.0533
0.7	1.481	3.077	0.0798
1.0	1.333	4.000	0.1333

Table 1. Minimum, maximum and incremental time for each modulation.

The exposure times discussed thus far are the totals for a given field. In order to demodulate the exposed image, a portion of the total exposure must be made using two beams, while the remainder is done using a single beam. The total exposure is given by:

$$\begin{aligned} t_{total} &= t_{2beam} + \frac{t_{1beam}}{2} \\ &= t_{2beam} + \frac{p \cdot t_{2beam}}{2} \\ &= t_{2beam}\left(1 + \frac{p}{2}\right) \end{aligned} \tag{4.2}$$

where p is the percentage of the two-beam time required to induce a given modulation, and is found by using equation (2.67). Once the two-beam exposure time is calculated from equation (4.2), the single-beam exposure time can be determined by multiplying the two-beam exposure time by p.

The individual exposures of the array for each modulation were made within 30 minutes to avoid variation induced by photoresist solvent out-diffusion and laser instability. A shutter, accurate to 10^{-6} sec, was used to precisely time each exposure. A secondary shutter was used to block one arm of the interferometer for the single beam exposure.

5.2 Interferometric lithography system

A tabletop two-beam interference system was developed to demonstrate the ability of interferometric lithography to synthesize defocus in a projection system. The tabletop interferometric system is capable of conducting both dry and wet exposures. The optical setup for wet exposures is facilitated by the use of a fused silica half ball. The interferometer schematic is depicted in Figure 19. The illumination source for the set up is an EX10BM 248 nm line narrowed excimer laser source, which is optimized by passing it through a beam expander, polarizer, and spatial filter before it enters the interferometer.

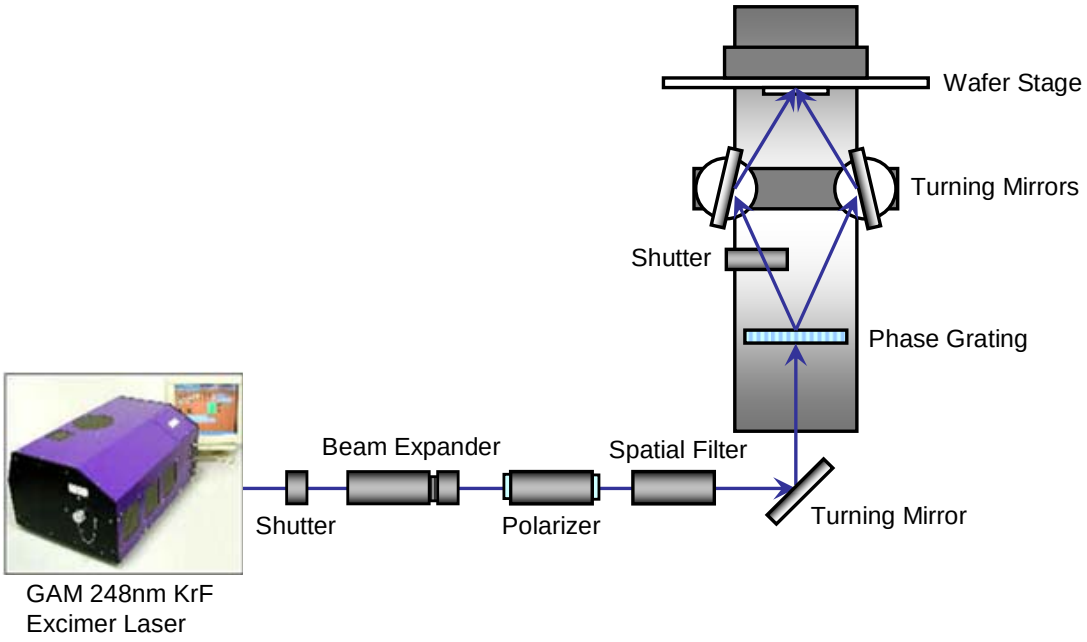

Figure 19. Table top lithography system for performing wet and dry interferometric exposures.

The 248 nm excimer laser was manufactured by GAM Laser, Inc. and was donated by Rohm and Haas Electronic Materials. The bandwidth of the laser is line narrowed using an unstable resonator, down to 10 pm and the spatial coherence is specified at 2 mm [15]. Additional specifications for the EX10BM may be found in Table 2.

Energy control range	8-20 mJ	**Energy stability (pulse to pulse)**	< 2% Std. Dev.
Max energy	20 mJ	**Temporal coherence**	5000 μm
Static gas life to 50% energy	90 days	**Spatial coherence**	2000 μm
Pulse length	15 ns	**Beam uniformity**	±5%
Beam size	8 x 3-5 mm	**Repetition rate**	40 Hz
Divergence	1 x 2 mRad	**Average power**	3/5 W

Table 2. Specifications for the EX10 Braggmaster 248 nm excimer laser [15].

Spatial coherence is critical to making the interference system more tolerant to misalignment. The source should be spatially coherent on the order of a few millimeters since the exposed field in this experiment was roughly 2-3 mm in diameter. A 5x beam expander fabricated by CVI Laser was utilized to expand the spatial coherence of the laser source. As a consequence of the beam expansion, the area over which the beam was spatially coherent was also magnified. The larger region of spatial coherence will provide better contrast when imaging, but may also introduce speckle in the final image. Speckle is the existence of ghost images and parasitic interference in the final resist image, which is generated from optics without antireflective coatings as well as from dust and debris on any optical surfaces. These conditions were averted by ensuring that all optical surfaces had antireflective coatings, and had been cleaned regularly.

Substrate material	UV grade fused silica	**Transmitted wavefront**	λ/10 at 633 nm 1 mm diameter beam
Transmission	> 97%	**Damage threshold**	1 J/cm^2, 8 nsec pulse at 248 nm
Housing material	Black anodized Aluminum	**Expansion ratio**	5x
Input aperture	4 mm	**Exit aperture**	20 mm
Housing diameter	31.8 mm	**Housing length**	97.1 mm

Table 3. Specifications for the BXUV-4.0-5x high energy UV beam expander [**16**].

As discussed earlier in Chapter 3, TE polarization is preferred to TM polarization since the modulation of TE polarized light is unity while the modulation of the TM state falls off with the cosine of the interference angle. A polarizer was used to separate TE and TM polarization states. The type of polarizer utilized in this study was a Rochon polarizer, which was obtained from Nova Phase [17]. A Rochon polarizer separates the two polarization states through the use of two single crystal prisms, which are cut, polished and glued together with their optical axes orthogonal to one another. A refractive index discontinuity is created at the interface of the two prisms due to the conflicting crystal orientations between each prism. The optical axis of the first prism encountered by a beam of light is perpendicular to the incident face of the prism. The polarization state of the beam that is oriented parallel to the optical axis of the second prism, or the ordinary ray, will see no change in refractive index and will continue on unaffected. However, the other polarization state, or extraordinary ray, will see the index discontinuity and diverge in accordance with the interface angle and the refractive index

difference. The divergence of the two beams allows for the selection of TE over TM polarization by using an aperture [10].

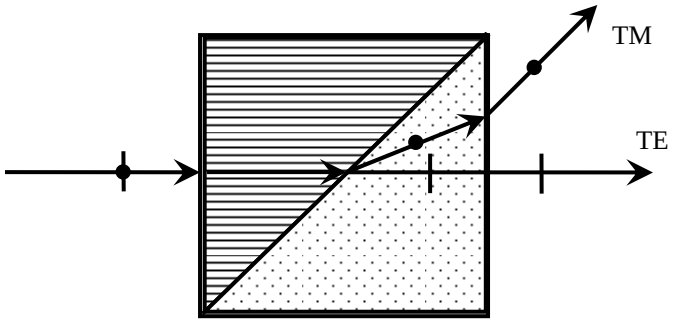

Figure 20. Configuration of the Rochon polarizer.

A spatial filter was introduced following the Rochon polarizer to "clean up" the beam due to a significant level of "ringing" and high-frequency noise evident in the resist image. "Ringing" refers to noise or unwanted multiple-order energy peaks in an otherwise smooth Gaussian beam [18]. The noise in the beam profile was found to have been caused by a number of sources, including dust in the air and on optical components, and Fresnel diffraction from the limiting aperture earlier in the system. The spatial filter removed most of the unwanted noise and passed only the primary diffraction order using two pinhole apertures (from Edmunds Industrial Optics) and an excimer grade fused silica spherical singlet lens (from CVI Laser). The lens specifications are given in Table 4 [19].

Substrate material	Excimer grade fused silica	**Diameter**	25.4 mm
Surface quality	10-5 laser quality	**248nm focal length**	152.1 mm
Thickness tolerance	±0.25 mm	**Radius**	77.3 mm
Concentricity	≤0.05 mm	**Surface figure**	λ/10 at 633 nm
Antireflective coating	≤0.25% per surface	**Dimensional tolerance**	+0 mm, -0.25 mm
Focal length tolerance	±0.5%	**Chamfer**	0.35 mm at 45°

Table 4. Specifications for the excimer grade fuse silica spherical singlet.

The spatial filter for this experiment is depicted in Figure 21, where the diameter of the TE output from the polarizer is reduced to 1 mm input beam diameter for the excimer grade singlet lens. The focal length of the singlet is ~152.1 mm at a wavelength of 248 nm, therefore the second pinhole is placed at that distance beyond the singlet to filter out any higher-order noise. An xyz-micrometer was utilized to precisely place the 50 μm pinhole at the focal point. A clean Gaussian beam is then passed onto the turning mirror to be redirected into the interferometer whose edges were not interfered with throughout the remainder of the configuration, which avoided introducing any additional noise to the beam.

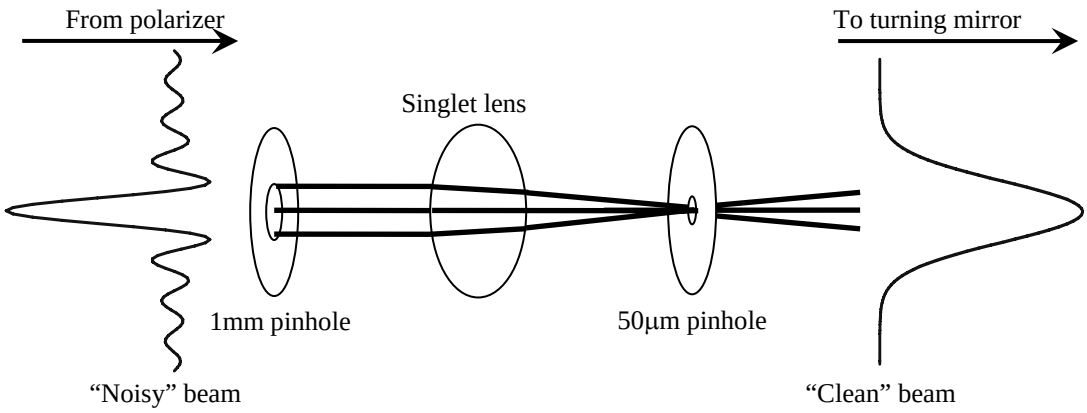

Figure 21. Spatial filter configuration with a 1mm input beam diameter and a 50μm pinhole at the focal point [18].

The following equations were used to determine the diameter required for the second pinhole [18]:

$$d = \left(1.5 \times 1.27 \times \lambda \times f\right)/D \tag{4.3}$$

where a wavelength λ = 248 nm, a focal length f = 152.1 mm and an input beam diameter D = 1 mm is assumed.

A 600nm-pitch chromeless phase shifting diffraction grating was used to split the Gaussian beam so that the resulting $\pm 1^{st}$ diffraction orders may be later interfered at the substrate surface [20]. This type of interferometer has been termed a "modified Talbot interferometer" since it uses a phase shift mask. In this configuration, turning mirrors have been added to allow for variable pitches. A phase shifting chromeless fused silica grating was used as a beam splitter because of its minimal complexity and it preserves beam energy. The phase-shifted grating was created by first writing the grating in chrome on a fused silica substrate and subsequently etching the pattern into the fused

silica using hydrofluoric acid. The chrome was stripped with a standard chrome etchant. The etch depth was previously determined for a 193 nm laser source to be roughly 2000 Å, however this depth is suitable for use with the 248 nm system. The drawback of utilizing a phase mask with an inappropriate etch depth is that the 0^{th} order is not completely suppressed, although it was an unexpected advantage since the 0^{th} order was very effective when aligning the interferometer. The diffraction angle of the 1^{st}-order beams depends on the pitch of the grating and the illumination wavelength, and is given by:

$$\theta_1 = \sin^{-1}\left(\frac{\lambda}{2 \cdot P_g}\right) \tag{4.4}$$

where P_g is the grating period and λ is the illumination wavelength.

The $\pm 1^{st}$ diffraction orders generated by the phase shift mask are redirected by two turning mirrors that are controlled by rotational micrometers. The diffraction orders are interfered at the image plane, whose rotation and vertical translation are also adjusted through the use of micrometers. The image plane rotation was adjusted to ensure that the imaging surface was orthogonal to 0^{th} order. The imaging plane was positioned so that the optical path lengths of each order were matched to one another. A variety of pitches are attainable by adjusting the height of the image plane and using the turning mirrors to redirect the beams so that they interfere at the new position of the image plane as pictured in Figure 22.

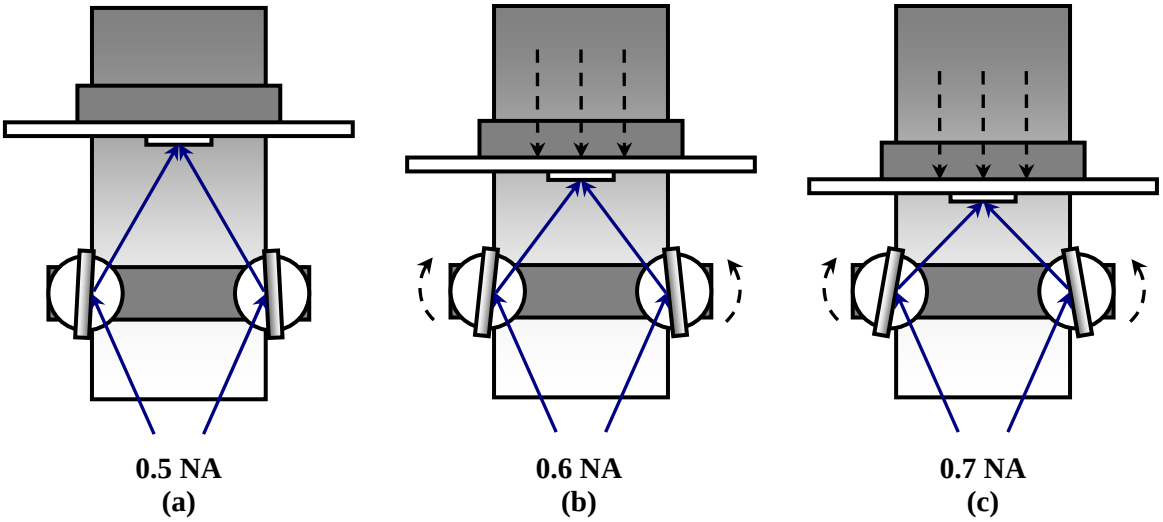

Figure 22. Pitch may be varied by adjusting the image plane and turning mirrors to the appropriate positions. NA's of (a) 0.5, (b) 0.6 and (c) 0.7 are pictured.

5.3 Substrate preparation and handling

Silicon wafers with a $\langle 100 \rangle$ crystal orientation were utilized as the substrate for this experiment. The $\langle 100 \rangle$ orientation facilitated the need to cleanly cleave the wafers into small rectangular pieces in order to conduct exposures. A 248 nm antireflective coating AR-2 was spun onto the wafers at 3000 RPM and baked at 205°C for 60 seconds. The targeted AR-2 thickness was ~70 nm. Shipley-95A photoresist material was then applied to the wafers at 2000 RPM and baked at 130°C for 60 seconds. The photoresist application was followed by a TSP 3-A top coating spun at 2000 RPM and baked at 90°C for 90 seconds, which prevented amine contamination and acid out-diffusion from the

photoresist. AR (Anti-Reflective) coatings and photoresists were provided by Rohm and Haas Electronic Materials, while the top coat was donated by TOK.

The coated substrates were cleaved into small rectangular samples to fit in the imaging plane of the interferometer. The samples were translated in the x-direction with each exposure generating an array of fields with varying exposure dose and synthetic defocus conditions. Following exposure the samples were post-exposure baked at 130°C for 60 seconds. The TSP-3A top coat was removed with the appropriate solvent and then the sample was developed in a Tetra Methyl Ammonium Hydroxide (TMAH) based developer solution for 60 seconds. The samples were finally rinsed with DI water, air dried and then moved along to the scanning electron microscope (SEM).

5.4 SEM image capture and analysis

An Amray SEM was used to obtain images of the developed interference pattern of lines and spaces on each sample. To avoid charging, a layer of gold was sputtered onto each sample for 10 seconds at a pressure of 100 mTorr prior to being loaded into the SEM. Each field was centered in the SEM viewing window and careful consideration was paid to viewing as close to the center of each field as possible. Five independent images were taken within close proximity to the center of each field at magnifications of 100,000x.

Each image underwent histogram equalization to normalize the images for the edge detection software. The edge detection software used for this experiment was

SuMMIT (SEM Metrology Interactive Toolbox), which was provided by EUV Technology LLC. Images were automatically calibrated by SuMMIT using an assumed pitch of 180 nm. The "Averaged Gradient" threshold method was used to detect the line edges, in which case the threshold is set at the maximum inflection point of the average of all the line edges in the image. The left and right edges of the lines were calculated independently by the software. A 10%-90% polynomial edge interpolation method was used to extract the edge position based on a polynomial fit to the edge data. Noise after the data interpolation was reduced by omitting outliers beyond 1σ. Five lines were measured per image and the average of each image was taken as one data point when analysis was conducted.

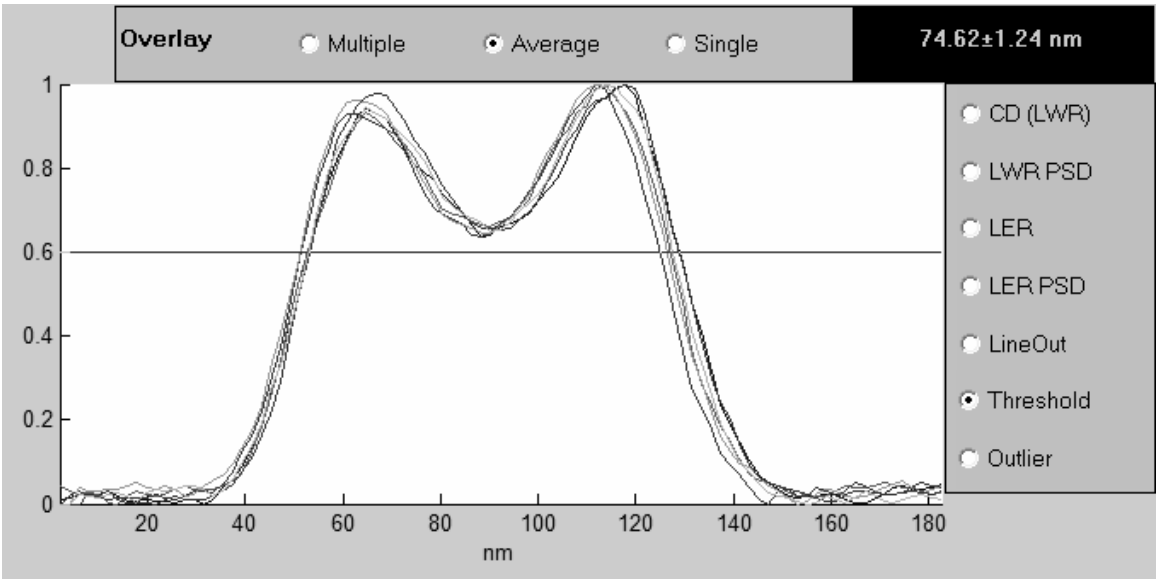

Figure 23. SuMMIT intensity profile of each of the five lines in a SEM image averaged through the length of the lines. The "Averaged Gradient" threshold is pictured at 0.6 for this particular image.

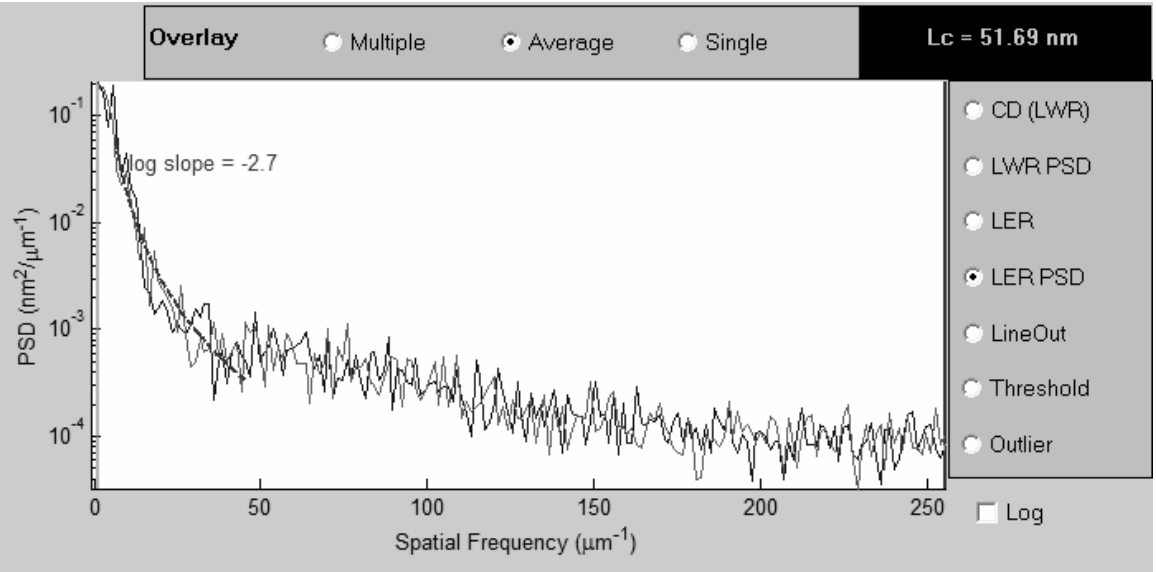

Figure 24. A sample of a SuMMIT line edge roughness PSD is pictured, which enables high order noise to be filtered out of the image so that accurate measurements of line width may be acquired.

6 Results

A range of photoresist exposures were conducted on the Talbot-Smith interferometer for induced optical modulations of 0.3, 0.5, 0.7 and 1.0. An NA of 0.70 was used to generate a pitch of 180 nm at an illumination wavelength of 248 nm, or an equivalent half-pitch of 90 nm. Levels of modulation below 1.0 were accomplished through the use of a secondary shutter that blocked one arm of the two-beam interferometer for a period of time determined by the desired induced modulation. CD measurements were collected from SEM images for each modulation over a predetermined exposure range and these measurements were plotted as a function of the exposure time. The following model was fit to the plotted data in order to extract the dose-to-size D_{Size} and the latent image modulation m:

$$\frac{D_{Size}}{D} = 1 + m(\xi) \cdot \cos\left(2\pi\xi \frac{CD}{2}\right) \tag{5.1}$$

where ξ is the spatial frequency of the exposed pattern and D is the exposure dose. The function in equation (5.1) can be attained by assuming a latent image intensity distribution given by:

$$\rho = \rho_o\left(1 + m(\xi) \cdot \cos(2\pi\xi x)\right) \tag{5.2}$$

in conjunction with the threshold development model, where ρ is the developable polymer in the latent image [21]. A summary of the results of the fitted CD data are given in Table 5.

Induced Modulation a_I	Measured Modulation *m*	Measured D_{Size} [sec]
1.0	0.73	1.48
0.7	0.48	1.62
0.5	0.29	1.70
0.3	0.17	1.98

Table 5. Summary of the extracted parameters from the threshold model fit of the CD vs. exposure time data.

The analysis used in this experiment assumes that the photoresist may be treated as a threshold detector. The polymer density ρ must surpass the threshold density ρ_o for the exposed latent image intensity to be considered developable, whereupon regions satisfying the condition $\rho > \rho_o$ will be removed. In Figure 25, the portion of the image intensity that is greater than the threshold of ρ_o is considered developable and will become spaces in the relief image.

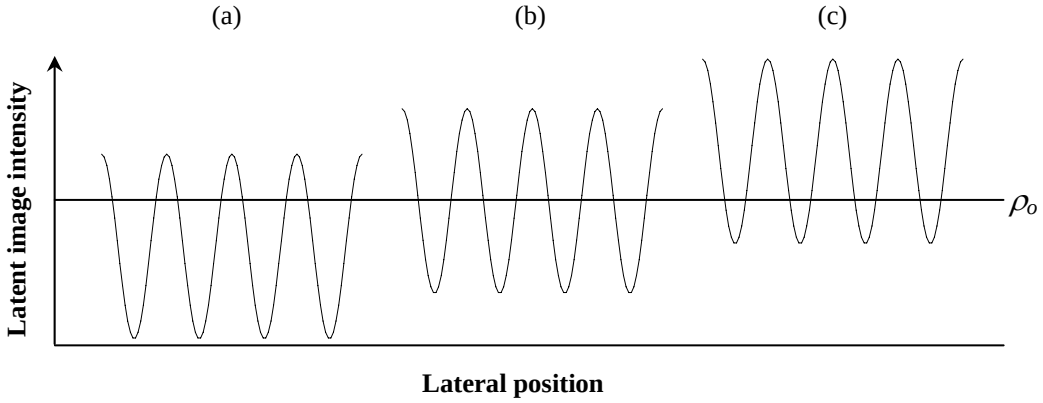

Figure 25. Latent image intensity for sinusoidal illumination where increasing exposure dose is pictured from left to right. The first condition (a) will result in wider lines than spaces, (b) will produce equal lines and spaces, and (c) gives narrower lines than spaces.

Many components contributed to the resist image modulation *m*, most of which were removed from the experiment (such as polarization and coherence) to simplify the analysis. However, due to the non-ideal nature of the experiment some of these modulation components were not entirely suppressed. TE illumination may have been assumed, but some TM illumination may have passed through the polarizer if its rotation were slightly offset. Furthermore, the illumination source was not entirely coherent and therefore some level of demodulation was introduced in this respect as well. One additional modulation component, the photoresist, was not discussed earlier. The induced aerial image modulation does not directly correspond to the latent image modulation extracted from the threshold model fit to the CD data due to the intrinsic modulation of the photoresist. The intrinsic modulation was estimated by assuming a linear fit to the relationship between the induced and the latent image modulations and was found to be approximately 0.70. This detail is shown in Figure 26:

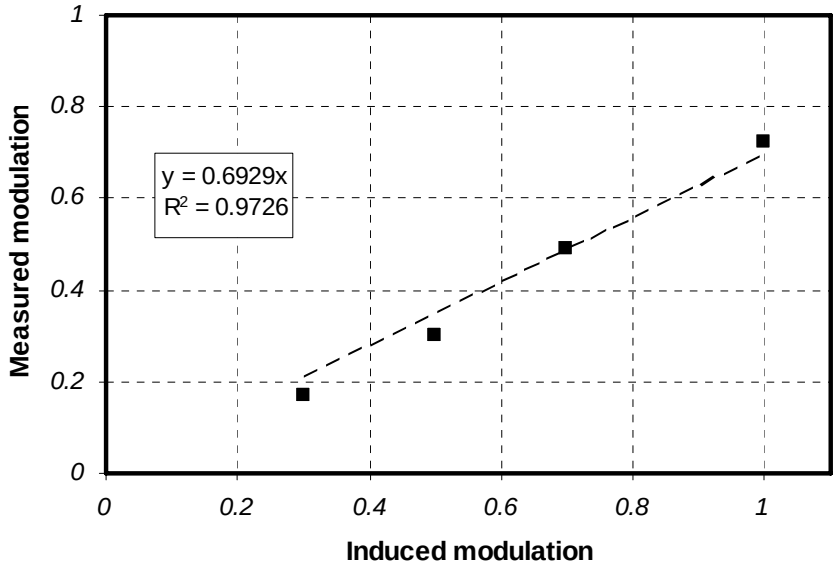

Figure 26. Relationship between the induced modulation a_I and the modulation m extracted from the CD data using a threshold fit. The linear fit has a slope equal to ~0.70 (intrinsic modulation).

As the modulation of the latent image intensity profile is decreased, the permissible exposure latitude decreases as well, which can be seen in Figure 27. Exposure latitude is said to decrease because the amplitude of the intensity profile at lower modulations is much smaller, and therefore there is a limited range of exposure adjustment that can be made before the resist is either entirely exposed or unexposed, latent image intensity completely above or below the threshold intensity, respectively.

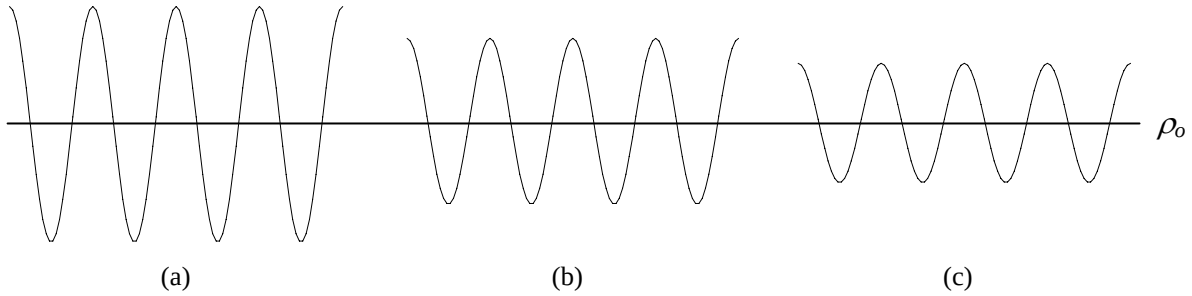

Figure 27. Latent image intensities are pictured for modulations of (a) 1.0, (b) 0.7 and (c) 0.5.

The exposure latitude (*EL*) is determined in part by taking the differential of equation (5.1) with respect to CD evaluated at the half-pitch:

$$EL = \left| \frac{\Delta CD / D_{Size}}{\partial CD / \partial D} \right| = \frac{\Delta CD}{CD} \frac{\pi}{2} m \tag{5.3}$$

The term ΔCD in equation (5.3) is the acceptable variation in the nominal CD. Experimental analysis was conducted for variations of 5, 10 and 20% from the half-pitch of 90 nm and the results are pictured in Figure 28.

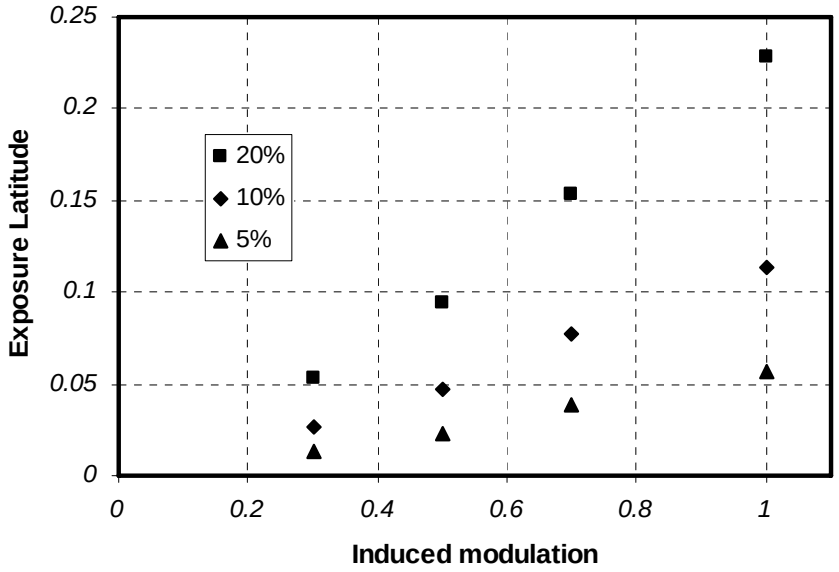

Figure 28. The attainable exposure latitude for acceptable variations in CD = 90nm of 5, 10 and 20% at four modulations.

Figure 28 shows a reduction in the exposure latitude with decreased induced modulation as expected. As the acceptable variation in CD is tightened, the attainable exposure latitude is also diminished.

In addition, the decrease in exposure latitude due to demodulation gives rise to a more rapid change in CD as exposure is varied. The rate of change in CD is attributed to the slope in the transition from peak to trough of the latent image intensity profiles in Figure 27. The slope increases for decreased modulations since the amplitude is reduced while maintaining the same frequency. The steep profile of the transitions in Figure 27 (a) allow for minimal CD variability as a function of exposure dose, while the shallower profile transitions in Figure 27 (c) will cause a much higher rate of change. An efficient metric for this phenomenon is the "normalized image log slope" (NILS), which (as its

name suggests) evaluates the slope of the aerial image profile. A larger value of NILS indicates a higher slope in the image profile, and in turn represents a higher quality resist image.

Samples of the SEM images from this experiment are provided in the following figures. The SEM images depict the range of exposure times used for each modulation to demonstrate the rate of change in the developed linewidth over that range. Due to the difficulty of reproducing the interference pattern at very low modulations, less data was available for the 0.5 and 0.3 modulations in comparison to modulations of 1.0 and 0.7.

The slope of the threshold model fit, which accompanies each set of images for each modulation, increases with decreasing exposure as expected. The 1.0 modulation fit had the smallest slope and examination of the SEM images will show a significantly small change in CD with exposure. The lines exhibit minimal roughness and there is no scumming evident. The 0.7 modulation was more heavily sampled across exposure and therefore more data was available. There is a slight increase in the slope of the fit and the presence of line edge roughness, however there is still no scumming in the resist image. As modulation is decreased to 0.5, not much data was available despite escalated sampling over the dose range. Line edge roughness is very apparent and there is scumming at the lowest dose. At the lowest modulation of 0.3 there is scumming across of all the exposed fields and the lines are very wavy. There was a great degree of difficulty in attaining quality images at this modulation.

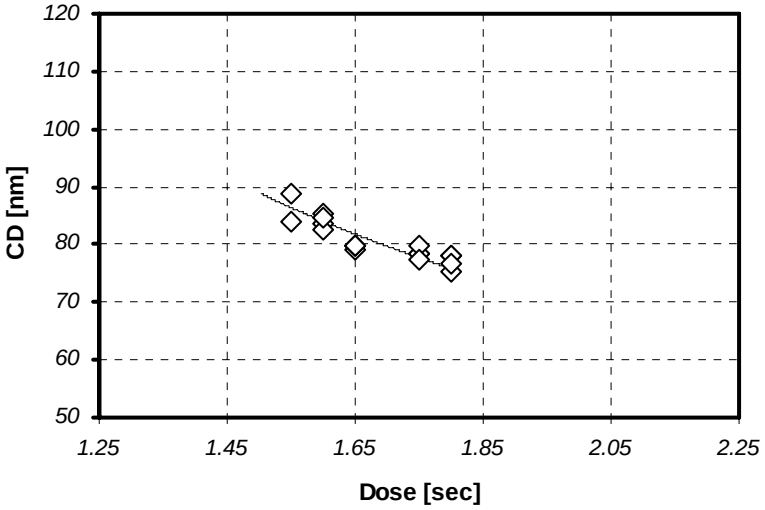

Figure 29. CD data for a modulation of 1.0. The threshold model was fit to the data and the parameters extracted were m = 0.73 and D_{Size} = 1.48sec.

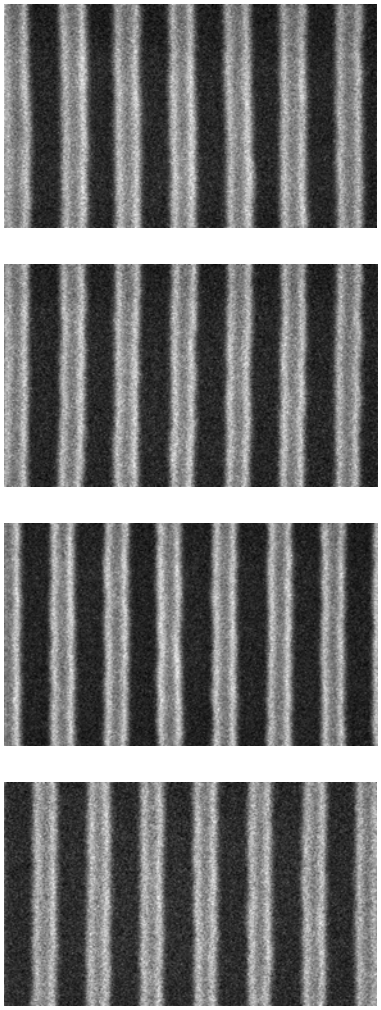

Figure 30. (Right) Exposure time increases with each image from top to bottom. Minimal line edge roughness is present. There is only a small change in CD with increased exposure, as expected.

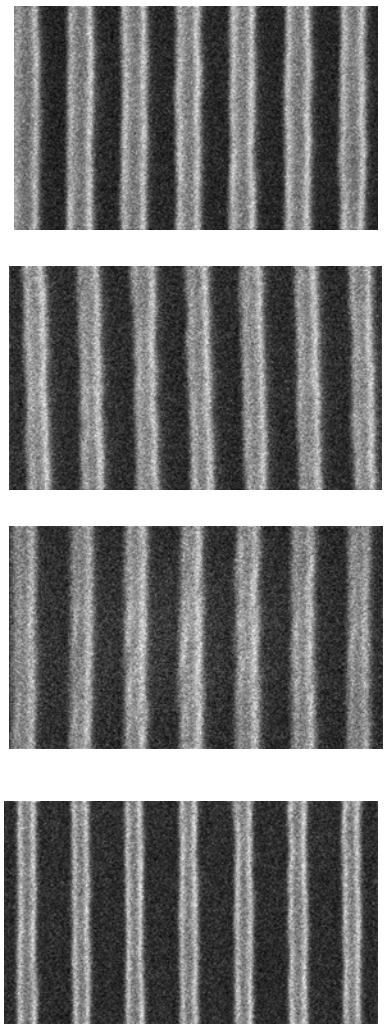

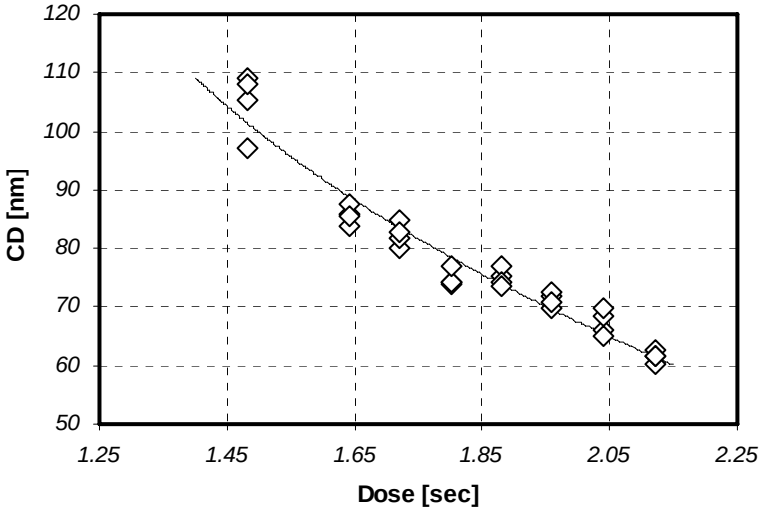

Figure 31. CD data for a modulation of 0.7. The threshold model was fit to the data and the parameters extracted were m = 0.48 and D_{Size} = 1.62sec.

Figure 32. (Left) Top to the bottom image, increasing increments of exposure time for the 0.7 modulation. Very little line edge roughness present. The images shown were chosen from a large sample in order to illustrate the stability of modulation over a large dose range.

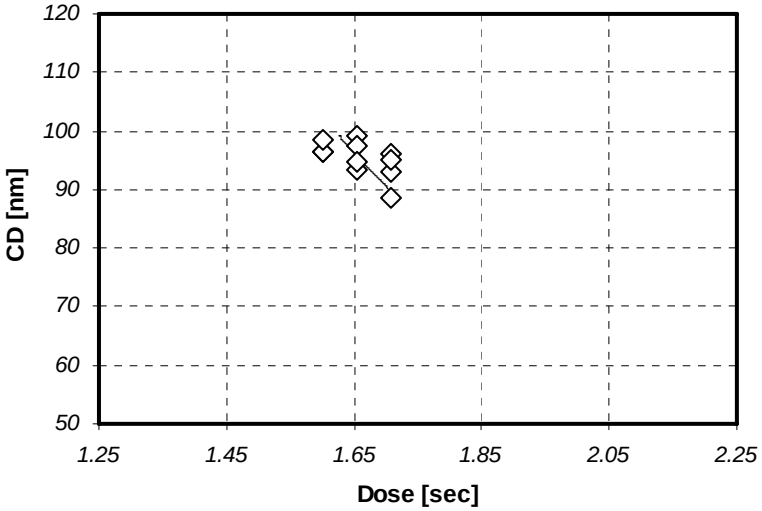

Figure 33. (Above) CD data for a modulation of 0.5. The threshold model was fit to the data and the parameters extracted were m = 0.29 and D_{Size} = 1.70sec.

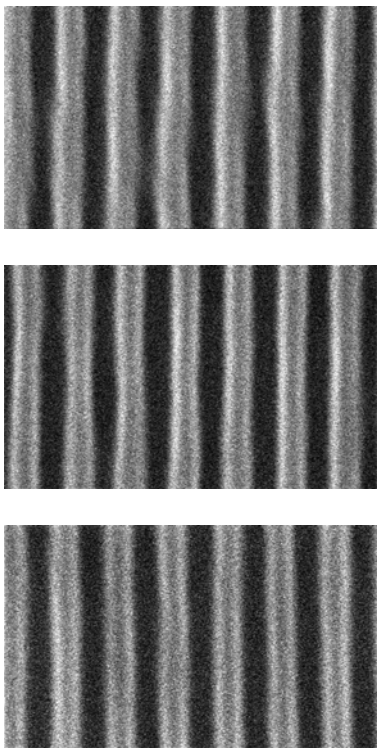

Figure 34. (Right) Moving from the top to the bottom image, increasing increments of exposure time for the 0.5 modulation. Line edge roughness due to demodulation is clearly present. Only a few good images were captured due to issues during resist processing.

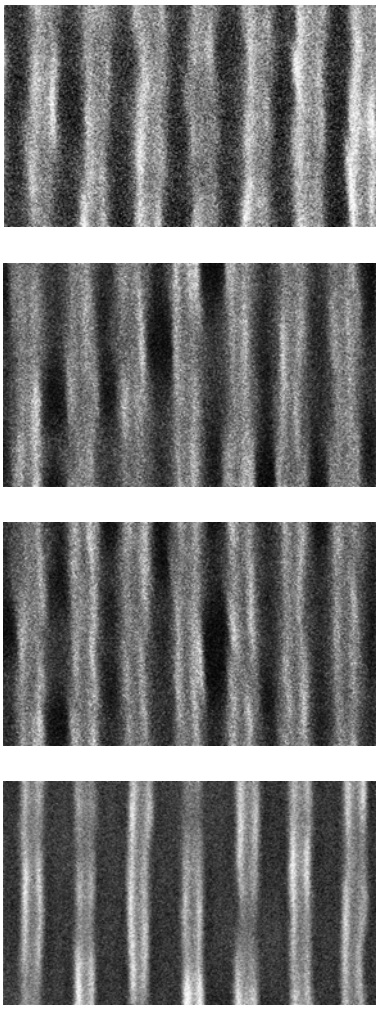

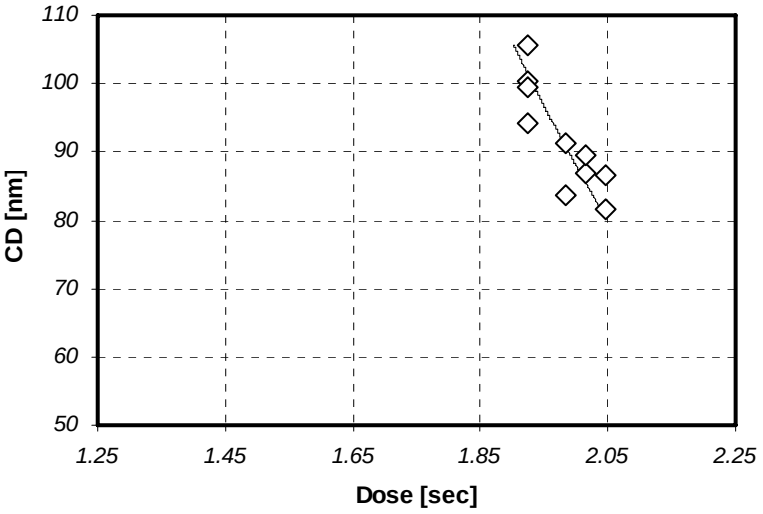

Figure 35. (Above) CD data for a modulation of 0.3. The threshold model was fit to the data and the parameters extracted were m = 0.17 and D_{Size} = 1.98sec.

Figure 36. (Left) From top to bottom, increasing increments of exposure time for the 0.3 modulation setup. There is a high degree of scumming and line edge roughness present in the pattern. Quality images were difficult to achieve at such a low modulation.

7 Conclusions

Interferometric lithography is capable of generating focus-exposure matrices to enable testing of new photoresist chemistries and RET's in development through the use of a synthetic focus generated by a second pass single beam exposure. The minimal complexity of this technique make it an attractive choice for the evaluation of emerging lithographic techniques, such as immersion, that would otherwise be cumbersome to reproduce experimentally. The defocused aerial image of a specified projection system may be synthesized by applying the appropriate single beam exposure, which is determined by matching the aerial image modulation of the interferometric system with the modulation of the defocused projection system. A modulation transfer curve (MTC) facilitated the transition from defocus to the single beam exposure required to generate the equivalent modulation in two-beam interference. Modulations of 1.0, 0.7, 0.5 and 0.3 were experimentally reproduced to demonstrate the ability of interferometric lithography to generate a variety of demodulations.

References

[1] Smith, B.W. and Sheats, J.R., eds., *Microlithography: Science and Technology*, ch. 3, Marcel Dekker, Inc., 1998

[2] Goodman, J.W., *Introduction to Fourier Optics*, McGraw Hill Companies, Inc., 1996

[3] Gaskill, J.D., *Linear Systems, Fourier Transforms and Optics*, John Wiley and Sons, Inc., 1978

[4] Mahajan, V.N., *Aberration Theory Made Simple*, ch. 1, 2, 8, SPIE – Optical Engineering Press, 1991

[5] E. Kintner, "Method for the calculation of partially coherent imagery", *Applied Optics*, **Vol. 17 No. 17**, 2747-2753, September 1978

[6] S. Subramanian, "Rapid calculation of defocused partially coherent images", *Applied Optics*, **Vol. 20 No. 10**, 1854-1857, May 1981

[7] B.J. Lin, "Partially coherent imaging in two dimensions and the theoretical limits of projection printing in microfabrication", *IEEE Transactions on Electron Devices*, **Vol. ED-27 No. 5**, 931-938, May 1980

[8] H.H. Hopkins, "The concept of partial coherence in optics", *Proc. Roy. Soc.*, **A 208**, 263-277, 1951

[9] H.H. Hopkins, "On the diffraction theory of optical images", *Proc. Roy. Soc.*, **A 217**, 408-432, 1953

[10] Guenther, R.D., *Modern Optics*, ch. 4, 6, 8-11, John Wiley and Sons, Inc., 1990

[11] Hecht, E., *Optics 4th Edition*, ch. 9-12, Pearson Education, Inc., 2002

[12] W. Hinsberg, F.A. Houle, J. Hoffnagle, M. Sanchez, G. Wallraff, M. Morrison, S. Frank, "Deep-ultraviolet interferometric lithography as a tool for assessment of chemically amplified photoresist performance", *J. Vac. Sci. Technol.*, **B 16 (6)**, 3689-3693, 1998

[13] J.A. Hoffnagle, W.D. Hinsberg, M. Sanchez, F.A. Houle, “Liquid immersion deep-ultraviolet interferometric lithography”, *J. Vac. Sci. Technol.*, **B 17 (6)**, 3306-3309, 1999

[14] J.A. Hoffnagle, W.D. Hinsberg, M. Sanchez, F.A. Houle, M.I. Sanchez, “Characterization of photoresist spatial resolution by interferometric lithography”, *Proc. SPIE.* **Vol. 5038**, 464-472 (2003)

[15] EX10 Braggmaster excimer laser specifications, GAM Laser, Inc. Orlando, Fl. 32822

[16] BX-4.0-5X High Energy UV Beam Expander, CVI Laser, LLC., Albuquerque, NM 87123

[17] UVRP UV Rochon polarizer, Nova Phase, 43 Sparta Ave., Newton, NJ 07860

[18] A. Pete, “Understanding spatial filters”, *Edmunds Optics Technical Support*, Edmunds Industrial Optics, Barrington, NJ 08007-1380

[19] PLCX-15.0-77.3-EUV-193 Excimer Grade Fused Silica Singlet Lens Spherical, CVI Laser, LLC., Albuquerque, NM 87123

[20] H. Kang, “New approaches in optical lithography technology for sub-79nm resolution, *PhD Thesis*, Rochester Institute of Technology (2004)

[21] A. Bourov, Y. Fan, F.C. Cropanese, B.W. Smith, “Photoresist Modulation Curves”, *Proc. SPIE.* **Vol. 5754** (2005)